Molecular dynamics study of scattering of nitrogen from a cryogenic nitrogen surface

Master's thesis in Chemistry by

Johannes Diedrich

Institute of Physical Chemistry

Research group of Prof. Dr. Ricardo Mata

Georg-August University of Göttingen

and

Institute of Aerodynamics and Flow Technology

Spacecrafts department, Rarefied Flows group

German Aerospace Center (DLR) Göttingen

May 2024

Examiner: Prof. Dr. Ricardo Mata

Second examiner: Dr. Martin Grabe

Abstract The non-equilibrium gas-surface interactions (GSI) between hot nitrogen gas and 4.3 K nitrogen ice were investigated. For this, molecular dynamics (MD) scattering simulations were carried out, comparing a flat and a rough aggregated surface model. The sticking probability and accommodation coefficients were determined for use in direct simulation Monte Carlo (DSMC) simulations. It was found that the sticking probability is similar for both models, but not unity despite the low wall temperature of 4.3 K and the accommodation coefficients correspond to partial accommodation. Additional focus is laid on uncertainty estimation, initial and final energy distributions and the modeled system size.

List of abbreviations

AC Accommodation coefficient.

AIMD *ab initio* molecular mechanics.

DLR Deutsches Zentrum für Luft und Raumfahrt, German Aerospace Center.

DSMC Direct simulation Monte Carlo.

EOM Equations of motion.

FF Force field.

GSI Gas–surface interaction.

LAMMPS Large-scale Atomic/Molecular Massively Parallel Simulator.

LJ Lennard-Jones.

MB Maxwell-Boltzmann (distribution).

MD Molecular dynamics.

ML Machine learning.

MM Molecular mechanics.

NPT Isothermal–isobaric ensemble.

NVE Microcanonical ensemble.

NVT Canonical ensemble.

PBC Periodic boundary conditions.

PDF Probability density function.

PES Potential energy (hyper)surface.

STG-CT High-Vacuum Plume Test Facility for Chemical Thrusters, Simulationsanlage für chemische Treibstrahlen Göttingen.

Contents

1 Introduction

1.1 Motivation

Understanding the flow and impingement effects of small rocket motor plumes is highly relevant for spacecraft design. It allows to assess contamination risks at spacecraft surfaces depending on their relative position to the thrusters.[1] While this is less relevant for commercial missions, e.g. cubesats, contamination is a major concern in missions that bear sensitive scientific instruments. One example is the planned lander mission to Jupiter moon Europa, where the exhausts especially during the final descent would significantly contaminate the landing site.[2] These contaminants (e.g. NH_3) could easily be mistaken for signs of life. But any other scientific instrument mounted on a spacecraft could possibly be disturbed by plume contamination, e.g. by discoloring.[3,4]
Such contamination effects are researched in large scale experiments at the German Aerospace Center (DLR) Göttingen in a unique test chamber called the High-Vacuum Plume Test Facility for Chemical Thrusters (STG-CT).[5] To mimic space-like conditions in a test chamber, any plume that misses targets must not scatter back into the chamber. Additionally, the test should be conducted under high vacuum during thruster operation. At a typical flow rate of $3\,\mathrm{g\,s^{-1}}$ for the operated rocket motors, substantial pumping is required to sustain vacuum during operation. For this purpose, experiments are conducted within a 1.6 m diameter, 5 m long cylindrical vacuum chamber with a helium cooled surface acting as a cryopump. By cooling the cylinder with boiling helium, a vacuum of 1×10^{-5} mbar during operation can be maintained. The residual pressure is the equilibrium H_2 pressure at the wall temperature of $4.2 - 4.7\,\mathrm{K}$. At these temperatures, all plume components except H_2 are assumed to freeze out at the chamber wall on first impact.
The rocket motor plume of a so-called monopropellant hydrazine thruster consists of the decomposition products of the catalytic and thermal decomposition of hydrazine over a heated Pt/Ir catalyst. Under full decomposition they are assumed to be 1:2 N_2 and H_2, but typically varying percentages of NH_3 are also present.[6] Alongside these main components, various side products of incomplete decomposition are present in reality. Indeed, the degree of decomposition of ammonia is a design parameter for this type of engine. For the present work, full decomposition is assumed and hydrogen is neglected, setting the focus on only the main component of the plume by mass, N_2.
The cryopump surface is approx. 20 years old technical copper. It can be assumed that it is rough, potentially porous and coated with various contaminants. Among these may be copper oxidation products, reaction products from incomplete hydrazine decomposition remains and water. Correctly representing this surface in simulations is clearly unfeasible. Instead, only the situation after some plume freeze-out has already happened will be discussed. It is assumed that the mass flow of a typical rocket motor is high enough to completely cover the surface with N_2 ice in the beginning of an experiment. Afterwards, the dominating interaction is only of the plume with the surface it originated.
In conjunction with experiments, the rarefied gas flow during operation is simulated using the direct simulation Monte Carlo (DSMC) method.[7–9] This is a coarse–grained method for simulating rarefied flows at kinetic scales. In this method, gas-wall interactions are described by statistical models called scattering kernels. The required parameters are usually derived by fitting either to experiment or to molecular dynamics (MD) simulations.[10]

Experimental data is not readily available for the case of the STG-CT, so the *ab initio* derivation from MD will be attempted. The model used in this work is the Cercignani-Lampis-Lord (CLL) scattering kernel[11,12] due to its simplicity and widespread use and implementation.
Due to the complexity of the real system, representing it in MD simulations is problematic. Different model choices for gas and surface could influence simulations to a large amount and in unforeseen ways. Instead of aiming for the most realistic representation, variations in the model should be compared for their effect on the scattering behaviour. This approach facilitates qualitative understanding over quantitative determination for a specific set of approximations. Only a very limited number of models is feasible within the context of this thesis, however. To do this, a baseline model is defined and a series of derived systems is simulated. The baseline model is designed to be as simple as possible: plume and ice consist of only molecular nitrogen and the surface structure is a flat cubic α phase single crystal at 4.3 K. The second structural model is a surface that is incrementally built up via deposition. The molecular projectiles for the deposition will be drawn from the same ensemble as the parametrization projectiles.
The main questions asked in this study are a) How accurate is the assumption of total freeze-out for the STG-CT wall? b) What are averaged gas-wall interaction parameters for the N_2 on N_2 system at typical operation parameters, under the above approximations? These questions shall be investigated using MD simulations of the scattering process, where a large number of individual trajectories of projectiles is analyzed. This workflow is used to determine the sticking probability s and to parametrize the CLL kernel. Special attention is given to uncertainty estimates for the determined parameters. Additionally, the minimum size of the slice of wall in such simulations is questioned. The process of sampling individual molecules from a gas ensemble by randomizing impact speed and angle is examined for its validity.

1.2 Current state-of-the-art

MD was previously used to study gas-surface interactions, an overview is given in Table 1.1. Many of the referenced works also determined sticking probabilities or parametrized scattering kernels. The general method typically involves the following aspects. The wall is built from the crystal structure and partitioned into layers, where the bottom-most is typically fixed, some are thermostatted and the rest moves freely. The projectile particle is sampled from some distribution or at concrete values of impact angle and energy. A large number of simulations is carried out over which the scattering behaviour is then averaged in post-processing. This work will attempt to adapt this methodology to the new system of the STG-CT cryopump wall. Contrary to most mentioned works, the sticking probability is of high interest as well additionally to the scattering kernel. As a consequence of the low surface temperature and resulting high sticking probability, the available number of data points for the scattering kernel is unusually low. While most previous studies argued that the wall sample size is unimportant, this work attempts to make an informed decision on system size based on observed impact effects.
Many of the previously published works applied the method to systems very different to the STG-CT problem. The surfaces modeled were often perfectly flat, which is very far from the reality of a technical copper surface covered with plume ice. Furthermore,

Table 1.1: Overview of systems studied in previous works where gas-surface scattering via MD was used to derive a sticking probability, scattering kernel or similar models. If several species were studied, only the ones most relevant to this work are given here. For the surface temperatures, only the lowest temperature considered is given here.

Authors	Gas	Surface	T_s / K	structure
Blömer et al. 1999[13]	N_2	Pt	50	flat
Bolton et al. 1999[14]	Ar	H_2O	0	flat
Yamanishi et al. 1999[15]	O_2	graphite	298	flat
Bruno at al. 2000[16]	Xe	GaSe	182	rough lattice
Yamamoto et al. 2007[17,18]	N_2	Pt	300	Xe adsorbate
Daun 2009[19]	N_2	graphite	3000	flat
Spijker et al. 2010[20]	Ar	Pt	300	flat[a]
Pham et al. 2012[21]	Ar	Pt	200	45° pyramids, deposited rough
Liang et al. 2013[22]	Ar	Pt(100)	300	flat
Gorji et al. 2014[23]	N_2	Cu(110)	650	flat
Reinhold et al. 2014[24]	N_2	hydroxylated silicon	300[b]	hydroxylated[c]
Mehta et al. 2016[25]	N_2	graphite	677	flat
Mehta et al. 2017[10]	N_2	graphite, quartz	300	unstructured fused quartz
Andric et al. 2018[26]	N_2	graphite	300	flat
Liang et al. 2018[27]	Ar	Pt	300	flat
Liao et al. 2018[28]	CH_4	graphite	350	incomplete upper layer
Andric et al. 2019[29]	N_2	graphite	300	flat
Nasab et al. 2019[30]	noble gases	DGEBA epoxy resin	300	rough
Liang et al. 2021[31]	Ar	Pt	150	flat
Liu et al. 2021[32]	Ar	graphite	500	flat
Nejad et al. 2021[33]	Ar	Au	300	flat
Wang et al. 2021[32]	Ar	graphite	300	flat
Nejad et al. 2022[34]	N_2	Ni	288	flat
Wu et al. 2022[35]	N_2	Pt	300	sinusoidal pattern
Brann et al. 2023[36]	CH_4	CH_4	20	flat[d]
This work	N_2	N_2	4.3	deposited rough

[a] However, all gas particles were simulated at once, so collision with adsorbed particles seems possible.
[b] also considered fully rigid surface.
[c] Flat single crystal surface, which on the atomistic scale is arguably rougher than e.g. a Pt surface.
[d] but includes random CH_4 orientation

cryogenic wall temperatures were rarely considered. Notably, the combination of both a cryogenic and a rough wall was found to be exceedingly rare. The surface materials tend to follow for which materials experimental reference scattering data exists (metal crystals or graphite), while the STG-CT surface is assumed to consist of the plume ice (rough N_2 with H_2 and NH_3 contaminants). The force fields sometimes included unphysical components like a returning spring force (Einstein lattice)[13,37] for the surface atoms or they were held in place completely rigid.[24] However, the distribution of energy through the slab is suspected to play an important role in scattering and adsorption-desorption mechanisms. For multiple collision impacts, the importance of the efficiency of energy redistribution in the lattice for the scattered projectile was already mentioned in the work by Bolton et al..[14]

Some works stand out as especially relevant. As shown in Table 1.1, the studies by Blömer et al.,[13] Bolton et al.,[14] Bruno et al.,[16] Pham et al.,[21] Liang et al.[27] and Brann et al.[36] considered surfaces below room temperature. Out of these, the recent work of Brann et al.[36] is the only example of a molecule scattering from cryogenic ice made from the same molecule. Furthermore they not only used a thermalized gas at some temperature but fast directed projectiles in accordance with their beam expansion experiments. This is a very close match to the rocket motor plume system, hence their results will primarily be comparable to this study. Some differences stand out, however. They considered the fixed impact angle 0° [1]. This work however will consider a distribution of impact angles, due to the complex distribution of impact angles found in the cylindrical chamber. The lowest impact energy they used (0.51 eV) is higher than what will be assumed for N_2 here, 0.23 eV. They also set the initial rotational energy to zero while in this work it is sampled according to the temperature of the plume, similar to the work by Andric et al..[29] The methane ice slab by Brann et al. was not built by deposition. Consisting of six molecule layers, the bottom three remained fixed, making for only three moving layers. They also did not simulate a periodic box and instead used artificially heavier molecules as boundaries. All other works mentioned concerning polyatomic projectiles, including this work, apply the rigid rotor approximation, while [36] consider molecular vibration. While the nitrogen bond is very stiff and therefore the rigid rotor approximation is robust, methane C-H bonds are weaker, so vibrational excitation up on collision is more likely. These differences could alter the scattering behaviour significantly, as more impact energy can be dissipated. According to a rheologic study of the two ices,[38] both materials show similar hardness and brittle failure between $5 - 30$ K. It is possible that the higher impact energy and the added effect of vibration have opposite effects and cancel to some degree. In the work of Bolton et al.,[14] Ar was scattered from a 0 K water crystal. The surfaces may be similar to some degree, except for water forming strong hydrogen bonds and therefore being a stiffer surface. Comparison to their work could become relevant if ammonia is introduced to the problem. They laid great focus on studying the dynamic effects of the impact on the lattice, inspiring some analysis methods used in this work. The study by Blömer et al.[13] was not considered for comparison due to the very small system size of their Pt surface.

Out of the works that considered rough surfaces, two stand out as particularly relevant for comparison. The work by Pham et al.[21] used deposited surfaces to simulate roughness.

[1] They report having run simulations with 45°, but do not give results from these except finding a lower s.

They did, however, consider the Ar-Pt system. Monoatomic systems lack rotational internal degrees of freedom, rendering the comparison to nitrogen flawed. The lowered Pt wall temperature of 200 K is noteworthy, but it is unlikely that it behaves similar to nitrogen at 4.3 K. The work by Mehta et al.[10] is interesting for comparison due to them studying a naturally rough surface with nitrogen as projectile at similar impact energies. However, they did not consider wall temperatures below 300 K. Their definition and analysis of DSMC parameters was partially inherited in this work.
This work will attempt to adapt the methodology to the new system of the STG-CT cryopump wall. Many aspects of the methodology were taken over to this work, notably the method of sampling a large number of single trajectories with given initial velocities and impact angles. Compared to the cited works, there are some notable differences. The sticking probability is of a high interest as well additionally to the scattering kernel. With the low surface temperature and consequential high sticking probability, the available number of data points for the scattering kernel is very low. An expandable workflow for surface deposition is developed to sample ice surfaces similar to how they would form from the freeze-out of the rocket motor plume. Special attention is given to the system size. While most previous studies argued that the wall sample size is unimportant, this work attempts to make an informed decision on system size based on observed impact effects. The process of sampling individual molecules from a gas ensemble by randomizing impact speed and angle is examined for its validity.

2 Theory

Using MD for scattering kernel parametrization is an interdisciplinary field between computational chemistry and rarefied gas flows aerodynamics. There are some differences in the vocabulary of the fields. The following sections discuss methods relevant for this work, in the order from abstract and macroscopic to concrete and atomistic. Finally, uncertainty estimation is discussed.

2.1 Isotherms

Consider a solid surface at some temperature T_s. Above the surface is a gas at some pressure p. The gas may adsorb onto the surface, building up a surface coverage θ. The surface may be flat, rough or porous, requiring different modelling approaches. Consequently, different definitions for the coverage may be appropriate. A *sorption isotherm* is a function $\theta(p)$ mapping some measure of surface coverage to the gas pressure.[39] A Master thesis project at DLR implemented the Langmuir isotherm into the SPARTA DSMC code.[40] Inspired by this model, it was originally thought that the process of plume freeze-out in the STG-CT could be modeled by an isotherm. After a literature review on isotherms, no option was found to make them applicable to the problem. One central assumption of isotherms is, as the name implies, a constant temperature during deposition and desorption and thus the fluid and the surface being in thermal equilibrium. This assumption is hard to justify with the plume from the 1000 K source impinging on the 4.3 K cryopump surface and then freezing out.
An additional complication is the definition of pressure. The nature of a cryopump is to reduce the temperature of the wall such that the gas equilibrium pressure drops to

negligible amounts. At $T_s < 5\,\mathrm{K}$, the solid nitrogen vapor pressure is negligible, as shown in Figure 6.1. However, the hydrogen vapor pressure is on the order of $10^{-5}\,\mathrm{mbar}$, which might influence the nitrogen adsorption in some way. The static pressure of the rocket motor plume greatly varies depending on the angle to the nozzle, but can reach several orders of magnitude more than the hydrogen dynamic pressure. As an alternative, scattering kernels (c.f. 2.3) were found to be applicable models, since they allow the temperature of the gas to change. Instead of pressure, they are functions of particle velocities.

2.2 Direct simulation Monte Carlo

The DSMC method was pioneered by G. Bird[7–9] in the 1960s. It is a probabilistic method for the simulation of rarefied gas flows. A gas is called rarefied if the particles' mean free path is longer than some representative length scale. This favors the treatment of the fluid as discrete particles over continuum fluid methods. There are some similarities to MD. In both methods the trajectory of point masses through position-momentum phase space is propagated. MD, however, operates on the nm-scale, while DSMC operates on the length scale of the mean free path. This scale changes substantially with the local number density. The method is therefore only realistically applicable for large scale problems in low density environments. While in MD the particle movement is deterministic and follows classical mechanics, DSMC particles interact statistically, where particle movement is separated into two parts: a) deterministic free flight, b) collisions. DSMC collisions are a stochastic, instantaneous change of velocity for selected collision partners. For each timestep, all particles that share a simulation cell may be randomly chosen as collision partners. In this process, they may exchange energy in any modes. In the DSMC context, particles are "simulation particles", a symbolic collection of real particles with approximately similar properties. They may represent a large number of real particles.
It is not within the scope of this work to apply the determined parameters to DSMC simulations or to describe the method in detail. For a more thorough review of the method, the reader is referred to the book by G. Bird.[9]

2.3 Scattering kernels

The following general discussion is adapted from Gorji et al.[23] A particle impinging on a wall is described by the two states before ($\boldsymbol{\psi'} = (v'_n, v'_{t_x}, v'_{t_y}, \omega'_1, \omega'_2)$) and after ($\boldsymbol{\psi} = (v_n, v_{t_x}, v_{t_y}, \omega_1, \omega_2)$) the collision. The velocity of the projectile in surface normal- and tangential direction is $\boldsymbol{v} = (v_n, v_{t_x}, v_{t_y})$ and the rotational state of a linear rigid rotor is given by $\boldsymbol{\omega} = (\omega_1, \omega_2)$. The apostrophe refers to initial conditions before the collision. Scattering kernels are functions $k(\boldsymbol{\psi}|\boldsymbol{\psi'})$ that give the probability of outcome conditions given the incident conditions. They are a form of probability density function (PDF). For the discussion of scattering kernels, the normalized coordinates $\boldsymbol{\phi'} = (\xi'_n, \xi'_{t_1}, \xi'_{t_2}, \Omega'_1, \Omega'_2)$ and $\boldsymbol{\phi} = (\xi_n, \xi_{t_1}, \xi_{t_2}, \Omega_1, \Omega_2)$ are introduced, with the normalized translational and rotational velocities $\boldsymbol{\xi} = (\xi_n, \xi_{t_1}, \xi_{t_2})$ and $\boldsymbol{\Omega} = (\Omega_1, \Omega_2)$.
Many scattering kernels exist, out of which the Maxwell kernel is one of the oldest and simplest. The CLL (Cercignani-Lampis-Lord[11,12]) kernel is commonly used in engineering DSMC simulations.[32,41] The CLL kernel improves on the Maxwell kernel by allowing

partial accommodation and typically matches experimental results qualitatively, but not quantitatively.[42] Among its shortcomings are the inability to describe coupling of internal energy (i.e. rotation) to translational modes.[23] Due to its common usage and implementation in codes like SPARTA, the CLL kernel is the most relevant kernel to parametrize for this work.

2.3.1 Accommodation coefficients

Scattering kernels typically feature parameters, usually determined from experiments or MD simulations. These parameters are often energy or momentum accommodations coefficients (ACs). In general, the energy AC is defined as

$$\alpha_E = \frac{E_i - E_f}{E_i - E_s}. \tag{2.1}$$

Momentum ACs (often denoted σ) are defined likewise and can be converted via $\alpha = \sigma(2 - \sigma)$. The suffixes mean i for initial, f for final and s for surface. E_s is a constant equal to the kinetic energy of the most probable velocity in the Maxwell-Boltzmann distribution at surface temperature. ACs are not defined for $E_i = E_s$. Because of the low wall temperature considered, it will generally be assumed that $E_i > E_s$, except stated otherwise. The AC states by how much the energy approaches the surface thermal energy after the scattering event. A value of 1 means full accommodation (i.e. diffuse reflection at wall temperature). $\alpha = 0$ describes an adiabatic event, i.e. specular reflection. The interpretation of values outside the 0, 1 range can be confusing. An overview of the value range is given in Table 6.1. Values larger than one are possible if the final energy is lower than that of the surface. Negative AC values are possible if the projectile gains energy during the process. While both outcomes are unlikely for the total energy, they may happen in individual degrees of freedom (modes).
When determining the AC from a finite set of individual simulations, there are different possibilities to derive a single averaged parameter from the distributions of initial and final energies. By taking averages of the energies, equation 2.1 can be formulated as a difference of means (equation 2.2) or as a mean of differences (equation 2.3). From here on, they are indexed 'diff.o.m.' and 'm.o.diff.' and are given by

$$\alpha^{\text{diff.o.m.}} = \frac{\langle E_i \rangle - \langle E_f \rangle}{\langle E_i \rangle - E_s} \tag{2.2}$$

and

$$\alpha^{\text{m.o.diff.}} = \frac{\langle E_i - E_f \rangle}{\langle E_i - E_s \rangle} = \frac{\langle \Delta E_{i,f} \rangle}{\langle \Delta E_{i,s} \rangle}, \tag{2.3}$$

respectively. The mean of a distribution is symbolized by $\langle\ \rangle$. Alternatively, the AC can be calculated for every E_i, E_f pair. The mean or median can then be determined from the resulting distribution of ACs.

2.3.2 Maxwell

According to the Maxwell kernel, there are two possible scattering outcomes: diffuse scattering or entirely specular scattering. It is defined by one parameter α, the fraction

of particles that are fully thermalized and diffusely re-emitted. The fraction of specularly deflected particles is thus $1-\alpha$. The Maxwellian PDF, which is a combination of the single-valued specular and the diffuse kernel, can be expressed as[23]

$$f^{\mathrm{M}}(\boldsymbol{\phi}|\boldsymbol{\phi}) = (1-\alpha)\delta(\boldsymbol{\xi}-\boldsymbol{\xi}'_R) + \frac{\alpha}{2\pi}\sqrt{\frac{m}{k_{\mathrm{B}}T_s}}\xi_z \exp\left(-\frac{m|\boldsymbol{\xi}|^2}{2k_{\mathrm{B}}T_s}\right), \tag{2.4}$$

with the Dirac delta function δ and the reflective velocity $\boldsymbol{\xi}_R = (\xi_x, \xi_y, -\xi_z)$ if z is the surface normal direction.
Its main shortcoming is the inability to describe partial accommodation. It is constrained to velocities either exactly equal to the incident velocity or equal to the Maxwell-Boltzmann distribution at wall temperature. Similarly, it is constrained to scattering angles either equal to the incident angle or to the cosine law of perfectly diffuse desorption. For systems with a hot gas scattering from cryogenic walls, it is unlikely that projectiles undergo specular reflection without energy exchange. Nor is it likely they are completely absorbed and diffusely re-emit at wall temperature of 4.3 K, unless it is H_2. The Maxwell kernel is therefore suspected to be unsuitable for application in this work.

2.3.3 CLL

The kernel by Cercignani and Lampis[11] with later modification by Lord[12] is given by

$$\begin{aligned} f^{\mathrm{CLL}}(\boldsymbol{\phi}|\boldsymbol{\phi'}) = {} & \frac{2\,\xi_n}{\pi^2\alpha_n\alpha_t\alpha_r}\exp\left(\frac{\left(\boldsymbol{\xi}_t - \sqrt{1-\alpha_t}\,\boldsymbol{\xi}'_t\right)^2}{\alpha_t(2-\alpha_t)}\right) \\ & \times I_0\left(\frac{2\sqrt{1-\alpha_n}\,\xi'_n\xi_n}{\alpha_n}\right)\exp\left(-\frac{\xi_n^2+(1-\alpha_n)\xi_n'^2}{\alpha_n}\right) \\ & \times \exp\left(-\frac{\left(\boldsymbol{\Omega} - \sqrt{1-\alpha_r}\,\boldsymbol{\Omega}'\right)^2}{\alpha_r}\right). \end{aligned} \tag{2.5}$$

Here, α_n, α_t, α_r are the energy ACs for normal, tangential and rotational energy of a fixed rotor and I_n is the nth order Bessel function.
The projectile kinetic energy is separated in two components, normal and tangential to the surface. Separate ACs α_{n}, α_{t} are used for these dimensions and α_{r} for rotational energy. Vibrational internal energy is neglected in this study, so the CLL kernel features three parameters. The tangential AC is given by

$$\alpha_t = \frac{E_{t,i} - E_{t,f}}{E_{t,i} - E_s}, \tag{2.6}$$

the normal AC by

$$\alpha_n = \frac{E_{n,i} - E_{n,f}}{E_{n,i} - E_s}, \tag{2.7}$$

and the rotational energy AC by

$$\alpha_n = \frac{E_{ri} - E_{r,f}}{E_{r,i} - E_s}. \tag{2.8}$$

2.3.4 Further models

Many extensions to CLL have been published.[23,27,43] In this work, they are not considered because they are not implemented in the SPARTA code[40] used at DLR at the time of writing.
The main shortcoming of such scattering kernels is the globality of the parameters. In this context, globality means that the kernel parameters are not a function of any projectile property, meaning projectiles of various angles or velocities will be handled with the same ACs. In the context of impact angles, this is also called isotropy of the kernel. This assumption could become problematic once the physics of the impact qualitatively change within the distribution. The kernel is an approximation to the mean scattering behaviour observed in the reference data, limited by the functional flexibility of the kernel.
To reproduce the observed scattering behaviour more precisely, a non-global mapping could be used. There are tradeoffs for the gained precision. While a global kernel can be used from one or a few numbers published elsewhere, sophisticated models require special training data, e.g. a MD database for the scattering problem at hand. Implementation of such models is also nontrivial, as available DSMC codes likely need to be modified. Some examples of fitting post-collision distribution of velocities have been published.[28,29,31–35] Some use Machine-Learning (ML) models or the PDF of the reference data is used directly.

2.4 Sticking probability

A scattering kernel is only concerned with particles that leave the surface. In the context of a cryopump, it is expected that most particles will aggregate on the surface. DSMC can handle this by deleting particles that hit the surface under certain conditions, governed by a probability parameter. This sticking probability is also a quantity that can be measured for real surfaces using the King and Wells technique.[44,45]
In MD, the sticking probability is determined by performing many simulations and counting how often the projectile either adsorbed (N_{sticking}) or scattered ($N_{\text{scattered}}$),

$$s = P(\text{sticking}) = 1 - P(\text{scattering}) = \frac{N_{\text{sticking}}}{N_{\text{sticking}} + N_{\text{scattered}}}. \tag{2.9}$$

A classification of MD trajectories is required to determine s statistically from a set of simulations. The specific criteria for these outcomes need to be defined carefully.
A particle is considered scattered once its distance from the surface exceeds the cutoff distance as used in the Lennard-Jones potential, 8 Å. A particle is considered to be fully accommodated to the surface ("sticking") when it does not fulfill the aforementioned condition within 50 ps. This value was chosen as a conservative guess based on values used in the literature in the range of 10 ps to 50 ps.[24,25,32,35,36] Inspired by the study by Bolton et al.,[14] an additional criterion for sticking is implemented to save computational effort. According to this criterion, the projectile total energy (kinetic + projectile–ice potential energy) needs to be lower than the desorption energy. This quantity is tracked with a moving average for the last 10 ps. If this mean falls below the desorption energy, the trajectory is counted as sticking. In ice models with defects and mixed phases with NH_3 and H_2, the desorption energy could prove hard to define and a conservative upper bound will be chosen.

2.5 Molecular Dynamics

For a comprehensive introduction to the topic, the reader is referred to the book by Tuckerman.[46] Furthermore, the following overview is based on [47]. MD is the propagation of a system of atoms or molecules in time via integration of the particles' equations of motion (EOM). The goal of such simulations is usually to estimate a property of the bulk material like phase transitions, structure and dynamic behaviour. At the start of any MD simulation, the system is initialized. This usually includes setting initial positions and velocities of all atoms and the parameters of their interaction. The core loop of the method is:

1. Calculate energies and forces
2. Numerically integrate equations of motion (apply timestep Δt)
3. Diagnostics and post-processing

The following overview approximately follows the same order.

2.5.1 Potential energy hypersurface and force fields

One of the most important aspects of MD simulations is the model that governs how particles interact with each other. This is closely related to the energy of the system, as the force acting on a particle can be inferred from the energy gradient. A scalar function for the potential energy with respect to all atomic positions, $V(\mathbf{r})$, is defined. It is referred to as the potential energy hypersurface (PES) or just the potential and contains central approximations.
To define a PES, the Born-Oppenheimer approximation is assumed. Because atomic nuclei are much heavier than electrons, the electrons move much faster. Thus, the nuclei are assumed to move in a field of electrons that instantaneously adapts to nuclear movements. Therefore, the energy of the system is given by the nuclear positions $\mathbf{r}$ without regard of electron coordinates.
It is a central approximation of any MD simulation and defines the physics that can and can't be represented. Therefore, the choice of methods used to calculate it greatly depends on the question that is sought to be answered by the simulation and the available computational power. There are various possible approaches.
If quantum effects need to be resolved and the system size and simulation time are low enough, methods of quantum chemistry can be used. This is called *ab initio* MD (AIMD). AIMD is relevant if electronic structure effects of the system are relevant, but the computational effort is much higher.
Molecular Mechanics (MM) is another possible approach where the forces between atoms are estimated based on their pre-defined bond situation and different parametrized potentials. Such potentials are called force fields (FF). The potential of the system is expressed as a sum over individual contributions:

$$V_{\text{total}} = V_{\text{bonds}} + V_{\text{angles}} + V_{\text{dihedrals}} + V_{\text{electrostatic}} + V_{\text{van-der-Waals}} + V_{\text{special}}. \tag{2.10}$$

Each term is a sum over all individual contributing particles. Depending on which species and phenomena are studied, only some of these contributions may be considered and with varying approximations.

For van-der-Waals interactions, a parametrization of the Lennard-Jones 6-12 potential (LJ) or related functions is common practice:

$$V_{\mathrm{LJ}} = 4\epsilon \left[\left(\frac{\sigma}{r}\right)^{12} - \left(\frac{\sigma}{r}\right)^{6} \right], \tag{2.11}$$

where ϵ is the zero crossing point of the potential and σ the equilibrium distance. All equations in this work are given in SI units unless stated otherwise.
For covalent bonds, parametrizations of the Morse potential

$$V_{\mathrm{Morse}}(r) = D_e \left(1 - e^{-\alpha(r-r_e)}\right)^2, \quad \alpha^2 = \frac{\mu\omega^2}{2D_e}, \quad \omega = \sqrt{\frac{k}{\mu}}, \quad \mu = \frac{m_1 m_2}{m_1 + m_2} \tag{2.12}$$

are often used. Here, D_e is the bond dissociation energy, μ is the reduced mass and k the spring constant of the bond. If only small deviations from the equilibrium bond distance occur, the harmonic spring is often used instead. Similarly, the potentials for angles and dihedrals can be approximated by simple parametrized functions.
If charged particles are included, their Coulomb potential

$$V_{\mathrm{electrostatic}}(\mathbf{r}) = \frac{1}{4\pi\epsilon_0} \sum_{i=1}^{N} \frac{q_i}{|\mathbf{r} - \mathbf{r}_i|} \tag{2.13}$$

for N particles with charges q_i at positions $\mathbf{r}_i$ is included as well. Since it is a long-ranged interaction, there is usually a cutoff after which it is indirectly solved, e.g. via particle mesh Ewald summation.[48]
The assumed requirement to the FF used in this study was reproducing reasonable structures and interaction energies at both $T_{\mathrm{s}} < 5\,\mathrm{K}$ and during impacts of the order of 1 eV. The the 5-atom rigid rotor model PHAST-N_2[49] was chosen. It was tested to correctly reproduce the different ice phases above and below 35 K while also giving accurate pressures and densities at 298 K. The choice was also biased by PHAST being a family of force fields for which H_2 was available. This facilitates easier extension of the method to mixed phase ices and parametrization of the H_2 scattering kernel in future work. Their potentials are given by

$$V_{\mathrm{PHAST}} = V_{\mathrm{LJ}} + V_{\mathrm{electrostatic}}. \tag{2.14}$$

The interaction sites and parameters are given in Table 2.1.
One pitfall of MM is the mixing of different parametrizations for different atom types. Let the LJ interaction parameters for atom types A and B be given by $\epsilon_{\mathrm{A}}, \sigma_{\mathrm{A}}$ and $\epsilon_{\mathrm{B}}, \sigma_{\mathrm{B}}$. Note that the parameters for each index describe the potential between atoms of that respective type only, therefore they are also sometimes written as e.g. σ_{AA}. The most consistent method of obtaining the interaction parameters for the pair AB would require to repeat the parametrization process with both particles. Instead, so called mixing rules are common approximations for the interaction between atoms A and B. The Waldman-Hagler mixing rules,[50]

$$\sigma_{\mathrm{AB}} = \left(\frac{\sigma_{\mathrm{A}}^6 + \sigma_{\mathrm{B}}^6}{2} \right)^{\frac{1}{6}} \tag{2.15}$$

$$\epsilon_{\mathrm{AB}} = \sqrt{\epsilon_{\mathrm{A}}\epsilon_{\mathrm{B}}}\, \frac{2\sigma_{\mathrm{A}}^3 \sigma_{\mathrm{B}}^3}{\sigma_{\mathrm{A}}^6 + \sigma_{\mathrm{B}}^6}, \tag{2.16}$$

Table 2.1: Parameters of PHAST-N_2 for WH mixing rules. With $\mathbf{R}$, the distance of the atom to the center of mass is given. The sites N2A correspond to the real nitrogen atoms, N2C (the center of mass) and N2F carry additional LJ interaction sites. The N2A and N2C sites carry charge, resulting in a quadrupole of approximately $\Theta = -1.514\,\mathrm{D\,Å}$.[49]

Site	M / Da	q_i / e	$\mathbf{R}$ / Å	$\frac{\epsilon}{k_\mathrm{B}}$ / K	σ / Å
N2C	0.000	1.0474	0.000	27.2601	3.4203
N2A	14.007	−0.5237	±0.549	0.0000	0.0000
N2F	0.000	0.0000	±0.784	15.3094	3.0777

were recommended for use with the FF employed in this work.[49][2]

2.5.2 Integration methods

The EOM considered in MD are usually not the ones originally derived by Newton. Instead, the Cartesian coordinates of all particles in the system can be described as generalized coordinates $\mathbf{q}$. This allows for coordinates like bond distances or bond angles to be used directly, making their integration and energy calculations easier. In analogy, generalized velocities can be defined as $\dot{\mathbf{q}}$ (Lagrangian mechanics). Instead of velocities, generalized momenta $\mathbf{p}$ can be defined instead. This idea is introduced in Hamiltonian mechanics. The tuple $\mathbf{q}, \mathbf{p}$ can then be seen as the coordinates in phase space of the system. The Hamilton EOM are

$$\frac{d\mathbf{q}}{dt} = \frac{\partial \mathcal{H}}{\partial \mathbf{p}}, \quad \frac{d\mathbf{p}}{dt} = -\frac{\partial \mathcal{H}}{\partial \mathbf{q}} \tag{2.17}$$

with the Hamiltonian $\mathcal{H} = T(\mathbf{p}) + V(\mathbf{q})$ which provides the total energy of the system. Note that everywhere else in this work, T refers to a temperature while here, $T(\mathbf{p})$ refers to the kinetic energy.
The integration of the EOM would be trivial if analytic integrals would exist. Since they do not exist, numeric integration is employed. For numeric integration, the problem is discretized into finite time steps $dt \equiv \Delta t$. Many different algorithms for numeric integration exist with advantages for different applications.
The integration algorithm used for discretization of the EOM should be symplectic. In the phase space of a system with any number of degrees of freedom, a high-dimensional equivalent of area within that phase space may be defined. A symplectic integrator is one that preserves this area. One major advantage of symplectic integrators is that conserved system properties, e.g. total energy, are more reliably conserved than with non-symplectic integrators like the Euler method or Runge-Kutta integrators. The methods discussed in the following are symplectic integrators.
Verlet integration is a symplectic first-order method. The order of a method states the highest order of derivatives that come up in the system of equations solved by it. The

[2] Contrary to the equation given in the PHAST-N_2 paper, Waldman and Hagler state a sixth root for σ_{AB} in their paper. The author assumes a printing error and follows the WH equation.

original algorithm published by Loup Verlet[51] did not calculate the velocities of particles, however. The Velocity Verlet integration[52] is an extension to the regular Verlet integration algorithm. It is a second-order method that calculates the velocities at every timestep. For MD simulations, they are a convenient quantity to have available, e.g. to calculate temperatures. In the general framework of positions $\boldsymbol{x}$, velocities $\boldsymbol{v}$, and accelerations $\boldsymbol{a}$, the Velocity Verlet algorithm states

$$\boldsymbol{x}(t+\Delta t) = \boldsymbol{x}(t) + \boldsymbol{v}(t)\Delta(t) + \frac{1}{2}\boldsymbol{a}(t)\Delta t^2, \tag{2.18}$$

$$\boldsymbol{v}(t+\Delta t) = \boldsymbol{v}(t) + \frac{\boldsymbol{a}(t)+\boldsymbol{a}(t+\Delta t)}{2}\Delta t. \tag{2.19}$$

The accelerations $\boldsymbol{a} = \frac{1}{m}\boldsymbol{F}$ are given by the particle masses and the forces $\boldsymbol{F}$. The latter are equivalent to the negative gradient of PES,

$$\boldsymbol{F}(t) = -\nabla V(\boldsymbol{x}, t) = -\frac{d\,V(\boldsymbol{x}, t)}{d\,\boldsymbol{x}}. \tag{2.20}$$

The original publication by Verlet also introduced the concept of neighbor lists. This is a method where for every particle, the indices of all its relevant neighbors in interaction distance are tracked and updated throughout the simulation. While initially adding overhead in computational effort and memory usage, this method may considerably speed up calculations. Interactions of particles that are far apart may be omitted entirely from direct interaction calculations. It is still used today and is also employed in this work.

2.5.3 Thermostats and barostats

For other ensembles than the microcanonical (NVE) ensemble, certain global properties like temperature and pressure need to be regulated. This task is not trivial and over the history of MD many different approaches were developed. In order to keep the temperature constant, a naive approach would be to periodically re-scale all velocities of atoms in such a way that the overall temperature is correct. Algorithms (thermostats) that implemented this approach include the Berendsen thermostat.[53] It was shown to violate the energy equipartition theorem, distributing energy from fast frequency modes to low- or zero frequency modes like translation, known as the flying icecube effect.[54] Instead of conserving total kinetic energy, the distribution of energy in all degrees of freedom, e.g. rotation, needs to follow the correct distribution to truly mimic the canonical (NVT) ensemble.
Other thermostats directly modify the EOM. The Langevin thermostat[55] introduces stochastic motion, mimicing Brownian motion. Nosé-Hoover thermostat chains[56] introduce additional degrees of freedom, equivalent to one or more heat baths, into the EOM. The latter has been shown to correctly sample the canonical ensemble. However, this approach is not derived from a Hamiltonian and can not be integrated with symplectic integrators.[57] For the rigid rotors considered in this work, Kamberaj et al.[58] derived symplectic integrators that correctly sample the canonical ensemble.
Algorithms constraining the pressure are called barostats. The Nosè-Hoover barostat[59] can both alter the EOM and scale the simulation box boundaries to regulate pressure.

2.5.4 Evaluation of trajectories

Because of the finite amount of particles and the resulting statistical noise, individual points in time are unlikely to be representative. In these cases, properties from MD simulations are averaged. Many properties, however, can be calculated during the simulation for every step or averaged over series of steps. To monitor the simulation progress and status, properties like temperature or special coordinates can be tracked.
The goal of a representative average is covering as much of the relevant phase space as possible, which can take enormous amounts of simulation time if certain parts of phase space are behind energetic barriers. An alternative approach to covering phase space involves a high number of parallel systems starting in different positions in said phase space.
The assumption that, given enough time the system will explore all of the accessible phase space is called ergodicity. In an ergodic system, averaging over time is equivalent to averaging over the ensemble. In this work, ergodicity is assumed for time averages of wall properties like its temperature.

2.6 Error estimation

2.6.1 Bootstrapping

Let $\mathbf{X} = (X_1, X_2, ..., X_N)$ be some data from which a statistic $\theta(\mathbf{X})$ (e.g. the mean) is calculated. If this data is normally distributed, the uncertainty of θ may be estimated using (multiples of) the standard deviation to obtain confidence intervals. The bootstrap[60] is a resampling method that can estimate the uncertainty of a statistic when the distribution of underlying data is not normally distributed. It is simple to implement and makes no assumption on the underlying distribution. However, it still makes assumptions:

- The data is seen as discrete (categorical) and only values that are in the original population are possible.
- Each data point contributes equally.
- The sample cumulative distribution function (CDF) of each bootstrap sample is the population CDF.

For data on an integer or continuous scale, the first point may be confusing. By intuition, if the data $x_1 = 4.1$ and $x_2 = 4.2$ were observed, it seems trivial that $x_3 = 4.15$ should also be possible. However it can be argued that all data are discrete once observed. Given the choice of assuming continuous but normally distributed or discrete and arbitrarily distributed data, the latter can be argued to produce more reliable uncertainty estimates.[61]
The third assumption can be understood as requiring that the given data is randomly sampled from its population. If the samples were systematically influenced to differ from their population, the bootstrap will not be able to infer that population.
A bootstrap is performed by drawing N times with replacement from the original data to create a new sample $\mathbf{X}_b$, for which the statistic $\theta_b = \theta(\mathbf{X}_b)$ can be calculated again. Doing this B times yields the bootstrap distribution of θ, from which an uncertainty can be inferred. In the case of the mean, it approaches the normal distribution by the central

limit theorem as B increases. The uncertainty of the statistic can be estimated as the standard deviation of this distribution.
The Bayesian bootstrap[62] is the Bayesian interpretation of the frequentist bootstrap. The two methods are closely related. From a Bayesian perspective, the classic bootstrap distribution is an approximation for the posterior of the Bayesian bootstrap. In implementation, the only difference between the Bayesian bootstrap method to the regular bootstrap is in the weights assigned to the data. The classic bootstrap weights correspond to the number of times n_i that data was drawn, $w_i = \frac{n_i}{N}$. The sum of these weights naturally sums up to one. However, they are discrete and bound to multiples of $\frac{1}{N}$. The Bayesian bootstrap assigns continuous weights from the Dirichlet$(0_1, ..., 0_N)$ distribution. This can be imagined as drawing $N-1$ random numbers between zero and one $\chi = \chi_0, ..., \chi_{N-1}$, sorting them, and appending zero and one to the beginning and end of the resulting list. The weight w_i is then the difference between the numbers χ_{i-1} and χ_i. The reason to include zero and one to the list is that the weights must sum up to one, which would not be the case if the differences $w_0 = \chi_1$ and $w_N = 1 - \chi_{N-1}$ were omitted. Another difference is that with low N, the classic bootstrap weights have a high probability to be zero. It can be argued that observed data should not be completely omitted in samples.

2.6.2 Standard error of the mean

If the statistic $\theta(\mathbf{X})$ is the mean, the central limit theorem states that in the limit of infinite samples, the distribution of θ will approach the normal distribution. This does not depend on the original distribution of $\mathbf{X}$. The uncertainty of the mean may be estimated from the standard error of the mean (SEM),

$$\sigma_{\langle x \rangle} = \frac{\sigma}{\sqrt{N}}. \tag{2.21}$$

Here, σ is the standard deviation of the population $\mathbf{X}$ and N the sample size. As more samples are considered, the mean is known to more certainty. This is not to be confused with the variability in $\mathbf{X}$ itself, measured by σ, as the distribution may be broad but its mean well determined.

2.6.3 Sticking probability

The sticking probability s is determined from categorical data, each trajectory is classified as either sticking or scattering. The Bayesian bootstrap is thus well suited for estimating the uncertainty of this parameter. With N trajectories classified as either "sticking" or "scattering", B Bayesian bootstrap samples are drawn, resulting in B new sticking probability samples $\mathbf{s}$. Their distribution is then described by the mean

$$\langle s \rangle = \frac{1}{B} \sum_{b}^{B} s_B \tag{2.22}$$

and standard deviation

$$\sigma = \sqrt{\frac{1}{B} \sum_{b}^{B} (s_B - \langle s \rangle)^2}. \tag{2.23}$$

The 95% confidence interval is then given by $\pm 1.96\sigma$.

2.6.4 Accommodation coefficients

The error of the ACs can be estimated by error propagation. The general equation

$$\Delta f(x_1, x_2, ..., x_n) = \left|\frac{\partial f}{\partial x_1}\right| \Delta x_1 + \left|\frac{\partial f}{\partial x_2}\right| \Delta x_2 + ... + \left|\frac{\partial f}{\partial x_n}\right| \Delta x_n \tag{2.24}$$

can be applied in two different ways depending on the exact definition of the AC. As discussed for equations 2.2, 2.3, a difference of means (diff.o.m.) or a mean of differences (m.o.diff.) can be used. In this work, these two definitions were numerically identical, but they produce different errors according to equation 2.24, namely

$$\Delta\alpha^{\text{diff.o.m.}} = \left|\frac{\langle E_f\rangle - E_s}{(\langle E_i\rangle - E_s)^2}\right| \Delta\langle E_i\rangle + \left|\frac{1}{\langle E_i\rangle - E_s}\right| \Delta\langle E_f\rangle + \left|\frac{\langle E_i\rangle - \langle E_f\rangle}{(\langle E_i\rangle - E_s)^2}\right| \Delta E_s \tag{2.25}$$

and

$$\Delta\alpha^{\text{m.o.diff.}} = \left|\frac{1}{\langle \Delta E_{i,s}\rangle}\right| \Delta\langle \Delta E_{i,f}\rangle + \left|\frac{\langle \Delta E_{i,f}\rangle}{\langle \Delta E_{i,s}\rangle^2}\right| \Delta\langle \Delta E_{i,s}\rangle. \tag{2.26}$$

All energies and energy differences are expected to be not normally distributed. In that case, the error of the means $\Delta\langle E\rangle$ and $\Delta\langle \Delta E\rangle$ may be estimated from Bayesian bootstrapping or via the SEM.
An alternative method to estimate the uncertainty of α is from its distribution. If α is calculated for every E_i, E_f pair, one obtains a distribution of ACs. From this, depending on its distribution, the standard deviation, SEM or bootstrap error can be calculated.

3 Methods

3.1 Simulation setup

All MD simulations were performed using LAMMPS.[63] The scattering simulations were ran in the NVE ensemble and integrated using Velocity Verlet.[64] Molecules were treated as rigid rotors within the `fix rigid/nve/small` style in LAMMPS. Time steps were 1 fs in scattering simulations and up to 5 fs in minimization simulations.
The PHAST-N_2 FF used involes charged particles. The Coulomb solver used was the `pppm/stagger` method[65–67] with a relative force accuracy of 10^{-6} and a cutoff distance for the direct solver of 8 Å.
Simulations were performed with full periodic boundary conditions. The box size in vertical (z) direction was chosen in such a way that, at minimum, the projectile was more than the Lennard-Jones interaction range ($r_{\text{LJ}} = 8$ Å) away from a surface in any direction. To make a consistent choice between all compared surfaces, additional space (1.5 times the regular size) was left free for the potentially less dense deposited surface. Additionally, two unit cells space for the thermostat and fixed layers in the deposition simulations needed to be left free. The final box height was

$$l_z = a\,(1.5 n_z + 2) + 2r_{\text{LJ}} + 2\,\text{Å} = 96.4\,\text{Å}, \tag{3.1}$$

where $n_z = 8$ unit cells was the baseline slab height and extra buffer was left to accommodate the total length of a PHAST molecule (1.6 Å). All projectile molecules were spawned at 9 Å above the surface.
Analysis of the results was performed using Python `3.11.5` and the packages NumPy 1.25.2,[68] SciPy 1.11.2[69] and MDAnalysis 2.6.1.[70,71] Visualizations were done using Matplotlib 3.7.2.[72]

3.2 Quantification of temperature and energy sampling

Several different temperatures can be defined in the context of an expanding rocket motor plume.

- Total temperature T_t
- Rotational temperature of the expanding plume T_{rot}
- Total translational temperature (thermal movement after subtracting the constant stream velocity), T_{trans}, can be split up into:
- Translational temperature in stream-direction (parallel component)
- Translational temperature normal to stream direction (normal component)

All except the last of these are some function of the distance to the nozzle.
In a rocket motor, the high internal energy (high bulk temperature) inside the nozzle is converted into a directed constant stream velocity and a lower translational (random direction movements) temperature. The fraction of those temperatures according to parameters of the nozzle and gas can be estimated by the isenthalpic relation[73]

$$\frac{T_{\text{trans}}}{T_t} = \left(1 + \frac{\gamma - 1}{2} M^2\right)^{-1} \tag{3.2}$$

where T_{trans} is the remaining translational temperature after expansion and T_t is the total temperature before expansion, $\gamma = \frac{c_p}{c_v}$ is the adiabatic index and M is the Mach number. This relation can be derived from the ideal gas law and some further assumptions, i.a. stationary flow and only one allowed direction of flow. Using typical values for monopropellant hydrazine thrusters as they are tested at DLR Göttingen, $\gamma = 1.4$ and $M = 6$, the fraction is 0.122. Since the total source temperature varies with different thrusters and their degree of hydrazine decomposition, no accurate general value can be selected. An estimation of $T_t = 1000\,\text{K}$ was selected as a generally valid typical value.
In a supersonic expansion, with increasing distance from the source, the number of particle collisions decreases until practically no energy is exchanged anymore. Rotational and translational temperature decrease until they freeze at different values.
To estimate a typical value of final rotational temperature for systems similar to monopropellant hydrazine thrusters in the STG-CT, an experimental measurement of the final rotational temperature of N_2 expansion[74] and G. Bird's theoretical estimation[75] were considered. The fraction depends on the distance between source and wall, therefore an accurate number is not easily available. If the scattering dynamics at a specific distance from the gas source is of interest, this ratio could be given with more detail. In this work,

a typical mean value of $\frac{T_{\text{rot}}}{T_{\text{trans}}} = 1.3$ was chosen. Therefore, the translational temperature will be estimated as $T_{\text{trans}} = 122\,\text{K}$ and the rotational temperature as $T_{\text{rot}} = 159\,\text{K}$. Discretizing this system is realized by drawing random samples from the distributions of its parameters. The speed of the projectile $v_{\text{projectile}}$ follows the constant stream velocity of the beam v_{stream}, modified by a random component v_T drawn from the Maxwell-Boltzmann distribution for one degree of freedom, $f(T)$.

$$v_{\text{projectile}} = v_{\text{stream}} + v_T. \tag{3.3}$$

The estimation of the constant stream velocity was derived from the estimate of T_t. A NASA report by Price and Evans (1968)[6] maps the stream velocity and bulk temperature of monopropellant hydrazine rocket motors to the degree of hydrazine decomposition (Fig. 2 there). From their data, the estimated value of 1000 K was used to determine the stream velocity at the same degree of hydrazine composition as $1259\,\text{m}\,\text{s}^{-1}$.

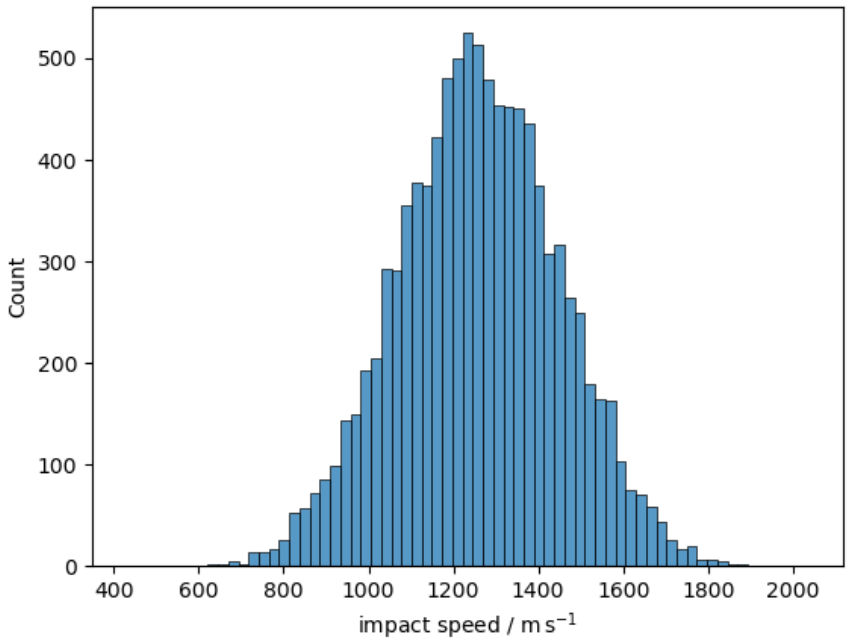

Figure 3.1: Distribution of velocities used for impact sampling. 10^4 samples with parameters $v_{\text{stream}} = 1259\,\text{m}\,\text{s}^{-1}$, $T_{\text{trans}} = 122\,\text{K}$.

The resulting distribution of speeds for 10 000 samples is shown in Figure 3.1. The distribution of rotational energy given some rotational temperature for a rotor with two degrees of freedom follows

$$E_{\text{rot}}(T_{\text{rot}}) = \frac{k_{\text{B}} T_{\text{rot}}}{2} \chi_2^2 \,, \tag{3.4}$$

where k_{B} is the Boltzmann constant and χ_2^2 is the chi-squared distribution for two degrees of freedom. In analogy, the distribution of translational energy is given by the χ_1^2 distribution, from which the distribution of speeds can be derived as

$$v = \sqrt{\frac{2E_{\text{trans}}}{m}}. \tag{3.5}$$

To represent a rocket motor plume with these properties in MD simulations, a sufficiently high number of individual single-impact simulations using discrete samples from the respective Boltzmann energy distributions needed to be averaged over. By performing single-impact simulations, it is assumed that individual projectiles will never come close to one another. This assumption can be supported by a brief order-of-magnitude estimation. With a rocket motor mass flow of $3\,\mathrm{g\,s^{-1}}$[5] and looking at only the nitrogen formed with full decomposition, the number of molecules impinging on the cryopump wall is $\dot{N} = 0.1\,\mathrm{mol\,s^{-1}}$. The mean particle number flow for the simulated area is then

$$\dot{N}_{\mathrm{sim}} = \dot{N} N_{\mathrm{A}} \cdot \frac{A_{\mathrm{sim}}}{A_{\mathrm{STG-CT}}} \approx 1000\,\mathrm{s^{-1}} \approx 1 \times 10^{-9}\,\mathrm{ps^{-1}}. \tag{3.6}$$

With simulation times of 50 ps, the mean time between impacts is therefore seven to eight orders of magnitude longer.

3.3 Baseline parametrization

The simulation parameters for the baseline model are summarized in Table 6.2.

3.3.1 Surface preparation

The unit cell was derived from the experimental crystal structure by R. W. G. Wyckoff.[76] Coordinates were scaled to relative coordinates, in which the center point and orientation of each molecule was inferred. Using this information, PHAST molecules were constructed with their corresponding pseudo atoms and atomic distances. The unit cells were then scaled to a cell parameter of $a = 5.6\,\text{Å}$. This value lies in-between the experimental one ($a = 5.644\,\text{Å}$[76]) and the one found for PHAST-N_2 ($a = 5.485\,\text{Å}$[49]), to allow for relaxation rather than expansion during minimization. The structure of the molecules themselves was kept constant and was checked to be not affected by scaling.
Initial slab geometries were generated in the form of LAMMPS data files by repeating the unit cells using `moltemplate.sh`.[77] The ice structure was minimized before further simulations using the following procedure.

1. 5 ps NVT dynamics at 4.3 K initial minimization.
2. 5 ps NPT dynamics at 4.3 K and 1 Pa for box relaxation.
3. 10 ps NVE dynamics as baseline.

For the first step, the Langevin thermostat as implemented in LAMMPS in `fix rigid/nve/small langevin` was used. It was chosen for stability and the effective cooling, as starting directly with NPT minimization would typically crash LAMMPS irrespective of the chosen cell parameter. Another reason is the random character of the method, allowing to repeat simulations from different positions in phase space by changing nothing but the random number generator seed.
In the second step, the Nosé-Hoover thermostat[56] and barostat were employed as implemented in LAMMPS's `fix rigid/npt/small`. The box was only allowed to change equally in the x and y dimensions and shrank by $1 - 2\%$.

The additional thermalization step was to allow the system to be integrated exactly like in the impact simulations. This way allows later comparison of thermodynamic properties to the unperturbed systems without any projectile, should the need arise.

3.3.2 Property sampling

In the scattering simulations, all system properties that are not model parameters in CLL needed to averaged out by sampling from distributions of values for each property. This is especially important for such properties that are not resolved at all in DSMC or fluids simulation, like molecule orientation, atomic-scale impact position on the surface or the specific state of the surface. Distributions were defined for every property and every individual simulation would sample from them using a different seed.
The distributions for translational and rotational energy of the projectile are given in 3.2. They are sampled from the respective temperatures T_{trans}, T_{rot} assuming Boltzmann distributed energies with one and two degrees of freedom, respectively.
The polar angle was drawn from a uniform distribution between 0° and 75°. A lower limit for the impact angle of $10^{[10,21]}$ – $15°^{[13,24]}$ or more is typical in the relevant literature and of practical reason for the simulations. The azimuth angle was drawn from a uniform distribution between 0° and 360°.
The impact position was sampled uniformly from the whole surface. With the random number n,

$$x_{\text{impact}}, y_{\text{impact}} = n l_{x,y}, \tag{3.7}$$

where $l_{x,y}$ is the length of the box in x or y direction. To determine a random rotation direction, the axis of rotation is chosen as a random angle φ around the N_2 bond axis. The two axes are orthogonal to maximize the moment of inertia. An angle of $\varphi = 0°$ corresponds to a rotation axis pointing towards negative z. The atomic initial speeds are given by the rotational energy as

$$|\mathbf{v}| = \sqrt{\frac{2E_{\text{rot}}}{r_i^2 I}} \tag{3.8}$$

where $|\mathbf{v}|$ is the COM-frame rotational speed of the N atom, r_i^2 is its distance from the COM (0.549 Å in PHAST-N_2) and I is the moment of inertia. These speeds are then mapped on the projectile atoms according to

$$\mathbf{v} = \pm|\mathbf{v}| \begin{pmatrix} 0 \\ \sin\varphi \\ \cos\varphi \end{pmatrix}. \tag{3.9}$$

The orientation of the projectile molecule is randomized by transforming the atomic positions and initial velocities with a random rotation matrix. The latter were sourced from the `scipy.rotation` package. Additionally, the state of the surface is randomized by running NVE dynamics for a random time from 0 to 50 ps.

3.3.3 Trajectory analysis

To determine the outcome of all simulations, they first need to be categorized into either sticking or scattering. Scattering is detected when the projectile returns to a distance from

the surface greater than the Lennard-Jones cutoff of the force field (8 Å), after which the simulation is aborted to save computational effort. Sticking is defined as the projectile not fulfilling the aforementioned condition after 50 ps. To further save computational effort, a stopping criterion for sticking is added, inspired by the study of Bolton et al.[14] The total energy of the projectile is tracked as the mean over the whole simulation. Once it drops below the desorption energy of α-phase nitrogen ice, 69 meV,[78] the simulation is aborted and counted as sticking. The reasoning is that the projectile has not had enough energy to emerge from the potential well for a considerable time.
For all simulations where scattering was detected, the initial and final velocity components of the projectile atoms were extracted for further analysis. Because the amount of data would be cumbersome, the full 10k scattering trajectories were not kept. Instead, the 3D velocity vector of the two projectile atoms $\mathbf{v}_{\text{proj},1}$, $\mathbf{v}_{\text{proj},2}$ were logged for each 0.1 ps frame. From this data, the COM velocity $v_{\text{proj}}^{\text{COM}}$ could be extracted as the mean of the atomic velocities for each dimension, respectively, because the masses are equal.

$$v_{\text{proj}}^{\text{COM}} = \frac{1}{2}\begin{pmatrix} v_{x,1} + v_{x,2} \\ v_{y,1} + v_{y,2} \\ v_{z,1} + v_{z,2} \end{pmatrix}. \tag{3.10}$$

From this vector the x and y components were used to determine the tangential kinetic energy E_t and the z component for the normal kinetic energy E_n. The projectile rotational energy E_r was calculated from its angular velocity ω as

$$E_r = \frac{I_{N_2}}{2}\omega^2. \tag{3.11}$$

Here, the moment of inertia of the PHAST-N_2 model, $I_{N_2} = 1.402 \times 10^{-46}\,\text{kg}\,\text{m}^2$, was used.

3.4 N_2 deposition simulation

N_2 is incrementally deposited onto a predefined α-N_2 surface of minimal depth. For the projectiles, the same energy distribution as in 3.3 was used, keeping all "sticking" classified molecules on the surface. As an additional stopping criterion, the temperature average over 2 ps needs to fall below 4.5 K. The binding energy criterion was adjusted to the same averaging time window.
Below the incrementally built ice, four additional atom layers (two unit cells) were included, taken from a previous minimized structure. Of these, the lowest layer was kept fixed. A rigid bottom layer avoids that the slab accumulates a downwards center of mass velocity. The remaining three layers were used as thermostat layers by integrating their motion with Nosé-Hoover NVT.
The deposition of molecules could lead to scattering and sputtering, so the number of simulations needed was not known beforehand. The surface was defined as finished when the same number of molecules as in the baseline model, 3200, were successfully deposited. As a final step, the thermostat and fixed layers below the aggregate were deleted and the z coordinates of the rest reset to start at zero height. Four surfaces were created this way differing in the sets of random seeds used to sample all projectile properties. These simulations needed to be run in serial unlike the scattering simulations, increasing runtime

from minutes to days. They were sped up by almost one order of magnitude by relaxing the presumably conservative long range force accuracy requirement of the Coulomb solver. Instead of 10^{-6} with the `pppm/stagger` method, 10^{-4} with the `pppm`[67] method was used. The switch in the used method follows the documentation of LAMMPS, which states that the prior is recommended for higher and the latter for lower force accuracy.

3.5 System size considerations

As Bolton et al. established in 1999[14] in the context of determining the sticking probability from MD simulations: "the rate of energy transfer away from the collision center [needs] to be taken into account". However in MD simulations, periodic boundary conditions (PBC) can cause artifacts, impeding energy dissipation in the lattice. To prevent this, the system size must be large enough, while size is limited by the computational effort. Two artefacts are considered: a) a rise in temperature in the whole slab due to the impact energy and b) the impact wave wrapping around the periodic boundary, re-entering the simulation and interacting with itself and the adsorbed projectile. The bottom of the ice may act as another reflecting boundary because the vacuum-facing layer can not propagate energy further downwards. In this way, the impact wave could artificially facilitate desorption. Generally, the instantaneous scattering process was observed to be faster than the global heating and the impact wave re-appearing at the site of impact. However, the mechanism of initial sticking and desorption shortly afterwards is possible and was observed in initial trial simulations.
The sticking criterion described in 2.4 was designed to correctly handle such cases and stop the simulation early when the desorption mechanism was no longer possible. An approximate goal for the minimum system size was set. The first is that within the 50 ps maximum simulation time, the ice should not heat up more than 1 K from a high energy impact. Secondly, the impact wave should be negligible by the time it reaches the box border at the sides and bottom.
Trial simulations with different sizes were compared to determine a sufficient system size (c.f. 4.7). The simulation parameters of these tests are summarized in Table 6.5. These simulations should represent an upper bound to the energy a projectile may deliver to the slab. It was found that for the flat surfaces used, the sticking probability was reliably 100% if the projectile was shot with zero angle into the exact simulation box center. This point, at any system size, always lied between surface molecules, facilitating energy uptake. Scattering only became a likely process if projectiles directly hit surface molecules. As an upper bound for the impact energy, $3000\,\mathrm{m\,s^{-1}}$ were chosen. No rotational energy was given to the projectile, as that could have increased the possibility of scattering.

3.6 Rotation energy fraction

The initial energy of the projectile can be distributed over translational and rotational degrees of freedom. Before parametrizing the baseline model, how much this distribution affects the sticking probability and ACs was tested. The simulation parameters of this test are summarized in Table 6.4. The impact position was sampled randomly from the

central unit cell. Given a random number n in the interval $(0, 1)$,

$$x_{\text{impact}}, y_{\text{impact}} = \frac{l_{x,y}}{2} - \frac{a}{2} + na, \tag{3.12}$$

where $l_{x,y}$ is the length of the box in x or y direction and a is the unit cell parameter. For this test, the projectile energy was fixed at 0.58 eV. Simulations were compared with all energy in translation ($v_{\text{stream}} = 2000\,\text{m}\,\text{s}^{-1}$ and with half of the energy in rotation ($v_{\text{stream}} = 1414\,\text{m}\,\text{s}^{-1}$). The simulation was performed at various fixed polar angles $\alpha = (15, 30, 45, 60)$. For each combination of angle and rotational energy fraction (0 or half), 400 simulations were carried out. The individual simulations differed in the seed used for their starting conditions, from which certain projectile properties were sampled.

4 Results and discussion

4.1 Deposited surfaces

The baseline and deposited surfaces were prepared according to the procedures described in 3.3 and 3.4, respectively. To avoid a systematic error, four surfaces were created via deposition, each differing only in the random number generator seeds used in each simulation. The resulting surfaces are compared to the baseline surface in Figure 4.1. A characterization is summarized in Table 4.1. For better visibility of their three-dimensional structure without the means of video, a Gaussian density surface mesh was rendered. The parameters for this mesh were a radius of 1.032 Å, an isovalue of 0.15 and 30% transparency. Generally, the deposition continued the α crystal structure and did not form many defects. Out of the four surfaces, two were found to have enclosed a hole and one surface had two holes. These holes were formed due to one molecule missing on its lattice site without visible perturbation of its surrounding. The deposition yielded rough surfaces due to incomplete layers. The height difference between surface atoms was three to five atom layers, equal to approximately two unit cells. According to the surface area of the mesh, the effective surface area increased by ca. 10% compared to the flat surface. The defects are not expected to be substantial enough to qualitatively change the speed of energy dissipation in the lattice, so any differences in sticking probability or ACs are expected to occur due to the roughness of the surface.

Table 4.1: Characterization of the surfaces simulated in this work.

Surface	Mesh surface area / Å^2	# of incomplete layers	# of holes enclosed
Baseline, Figure 4.1a	7298.53	0	0
Deposit 1, Figure 4.1b	8036.55	4	2
Deposit 2, Figure 4.1c	8000.70	5	1
Deposit 3, Figure 4.1d	7966.77	3	0
Deposit4 , Figure 4.1e	8061.69	3	1

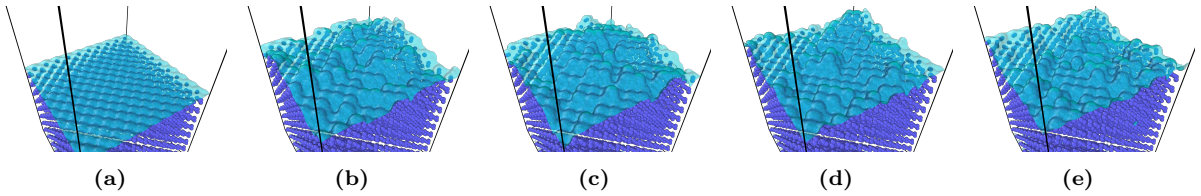

(a) (b) (c) (d) (e)

Figure 4.1: Images of the surfaces. An isosurface mesh is rendered to highlight the three-dimensional structure. From left to right, the baseline model (a) and the surfaces of the deposited model (b-d). The images of the deposited surfaces look higher because they still contained the four artificial bottom layers that were deleted before scattering.

4.2 Sticking probability

For all five surfaces, 10 000 scattering simulations were performed. The sticking probability was then calculated according to equation 2.22. The uncertainty was estimated via Bayesian bootstrapping with 10^4 bootstrap samples. This distribution in s was found to be approximately normally distributed, so the standard deviation was used to determine 95% confidence intervals as $\Delta s = 1.96\sigma$. The outcomes are summarized in Table 4.2.

Table 4.2: Outcomes of 10 000 trajectories for each surface and the resulting sticking probabilities. Uncertainties in parentheses are the 95% confidence interval (1.96σ) after $B = 10^4$ bootstrap samples.

Surface	N_{sticking}	$N_{\text{scattered}}$	s
Baseline, Figure 4.1a	9842	158	0.984(3)
Deposit 1, Figure 4.1b	9823	177	0.982(4)
Deposit 2, Figure 4.1c	9881	119	0.988(3)
Deposit 3, Figure 4.1d	9752	248	0.975(4)
Deposit 4, Figure 4.1e	9823	177	0.982(4)
Deposit total	39279	721	0.982(2)

The sticking probability of all surfaces was found to be very high. The difference between the baseline and deposition models is minimal and covered by the confidence interval. There appears to be a trend that the deposited surfaces make for slightly lower sticking probabilities, with ¾ of the test surfaces being below the baseline value. Between the surfaces of the deposition model, the discrepancy is higher than the confidence interval. This shows the importance of taking several sampled surfaces into account can be seen. If, by chance, only deposit surface 2 (Figure 4.1c) would have been evaluated, the observed trend would be opposite. This indicates that the statistical noise between the surfaces is higher than the calculated confidence interval suggests. From here on, if not mentioned otherwise, all discussions of the deposited surface(s) consider the entirety of the data from the four sampled surfaces.
Bisschop et al.[78] measured a lower limit for N_2 sticking to N_2 at 14 K of $s \geq 0.85$, although for 300 K thermal projectiles. All findings in this work are in agreement to this lower limit. Brann et al.[36] (c.f. Table 1.1) measured the sticking probability for CH_4 sticking to 20 K CH_4 and found $s = 0.97$ via experiment and $s = 0.91$ via MD simulations. The

lowest impact energy they used was 0.49 eV. While it might be surprising that this work matches their experiment better than their MD simulations, this is likely attributable to a combination of the differences between the considered models as discussed in 1.2. Notably, their consideration of methane and including vibration might allow for more impact energy being redistributed into internal energy, increasing s compared to nitrogen. On the other hand, the use of double the impact energy likely decreases s. In work by Thompson et al.,[79] the sticking probability was measured directly for methane on various 33.5 K D_2O morphologies. They considered different impact energies and found $s = 0.90$ at 0.27 eV, the closest match to this work, for crystalline CD_4. Unfortunately, none of the three experiments allows direct comparison to this study due to the differing impact energies, species or wall temperatures. The results of this study indicate a higher s than the cited MD simulations, which qualitatively matches the expected trend for a lower impact energy and lower surface temperature.
Thompson et al.[79] also studied the effect of surface structure. In their experiment, only beyond impact energies of 0.5 eV did the surface structure make a strong difference. And even then, only a porous material had a qualitative effect on s, while the difference between crystalline and amorphous ice was small. The deposited surfaces simulated here did not form an amorphous structure, but they seem to support this result at least for rough surfaces. For the case of the STG-CT, this means that the exact structure of the ice might play a diminishing rule for N_2 freeze-out. The results indicate that the lower limit of $s \geq 0.85$ might be conservative and it is to be expected that up to around 2% of nitrogen molecules will scatter at least once. However, these results all follow the assumption that only nitrogen is present in the ice. Mixed phases with hydrogen and ammonia might shift these results. The surfaces simulated in this work were close to ideal crystals despite the deposition method. A mixed species surface might be less structurally ordered and therefore less able to redistribute the impact energy. As a consequence, scattering and sputtering might be more likely. Additionally, hydrogen is less strongly bound to the surface and could be sputtered more easily by heavier projectiles. It is therefore assumed that the results of this work represent an upper bound to the sticking probability in the experiment.

4.3 Scattered energy distribution

The velocities of scattered projectiles were extracted from all trajectories. From the latter, the kinetic energy components normal and tangential to the surface normal vector $\begin{pmatrix}0 & 0 & 1\end{pmatrix}$ were calculated. In the work by Brann et al.,[36] the final velocity distributions were found to follow the Maxwell-Boltzmann (MB) distribution. This was investigated by fitting the PDF with the respective number of degrees of freedom f to each mode using linear least squared regression. To also include the final rotational energy, the final energy components were considered instead of the velocity. The degrees of freedom assumed for the normal, tangential and rotational energy components were $(f_n, f_t, f_r) = (1, 2, 2)$. With the dimensionality fixed, the only varied regression parameter was the temperature. The distributions and the fits are shown in Figure 4.2. The fits for normal and rotational energy qualitatively match the data. For the tangential energy, the match is poor in the baseline surface and slightly off for the deposited. The difference between the two could be accounted for by statistical noise, as the latter has four times the data. Still, the

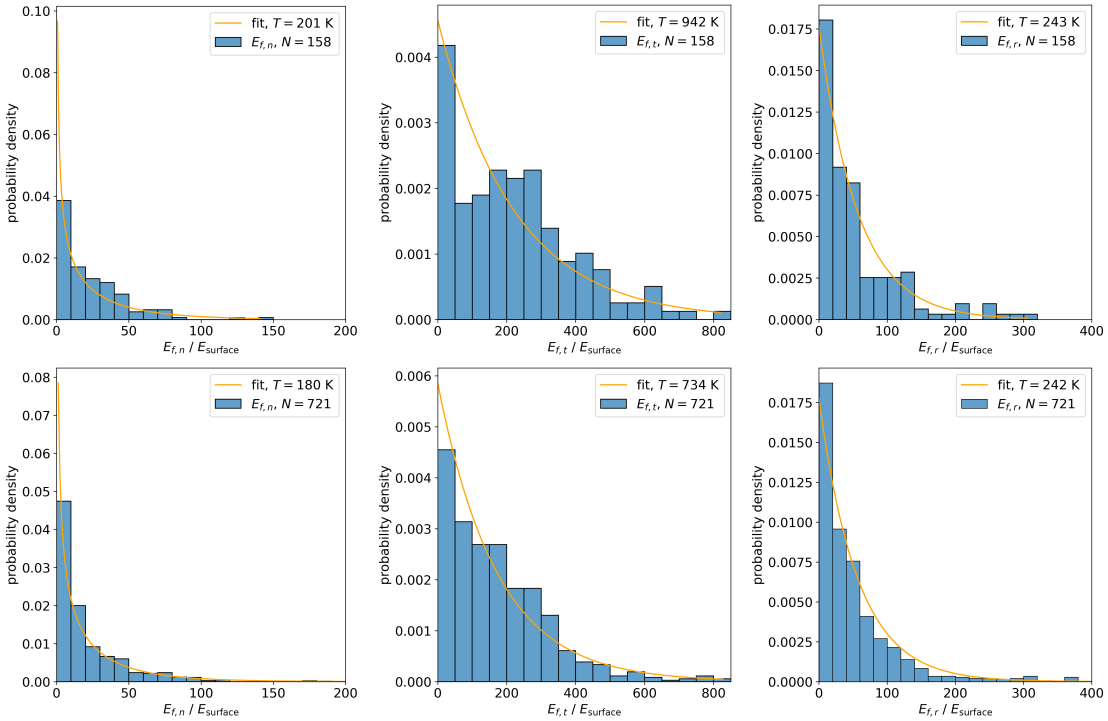

Figure 4.2: Final energy distribution of all projectiles that underwent scattering. The energy is given in units of multiples of the wall thermal energy, 0.37 meV. From left to right, the normal, tangential and rotational energy distribution are shown. Top row: baseline surface; bottom row: deposited surface. Fitted Maxwell-Boltzmann distributions are shown as well.

tangential energy seems to not quite follow the MB distribution, with more probability density at medium and less at low energy.
The temperatures obtained from the fits can be compared to the initial temperature components of the projectiles. With the mean impact velocity of $1259\,\mathrm{m\,s^{-1}}$ (corresponds to $T^{\text{initial}} = 2670\,\mathrm{K}$), it can be estimated how much energy the projectiles exchanged with the surface. The fraction $\frac{T^{\text{fit}}}{T^{\text{initial}}}$ approximates how much energy was retained, so $1 - \frac{T^{\text{fit}}}{T^{\text{initial}}}$ is an approximation to the energy AC in the case of a 0 K wall. The data for this approximation are shown in Table 4.3.

Table 4.3: The approximation $1 - \frac{T^{\text{fit}}}{T^{\text{initial}}}$ to the AC from the scattered energy distributions.

Surface	normal	tangential	rotational
Baseline	0.925	0.647	-0.53
Deposit total	0.933	0.725	-0.53

According to this approximation, the projectiles lose most normal energy upon the impact, coinciding with the high sticking probability. Some tangential energy is retained and the projectile is likely to gain rotational energy from the impact. It should be noted that this approximation is flawed, since the initial state of the plume is not equivalent to a gas at

2670 K. However, the results match the calculated ACs (c.f. Table 4.4) remarkably well.

4.4 Accommodation coefficients

The accommodation coefficients were calculated according to 2.3.3 and are summarized in Table 4.4. Due to the high sticking probability, the amount of available data points is low compared to a typical numbers of trajectories used in literature (≈ 2000[29,36]) to parametrize a scattering kernel. The baseline and deposited surface data differ to a factor of four in available data. Therefore the latter are expected to be determined to higher confidence. If higher confidence were needed, more scattering simulations could be performed. The computational costs of the present data set sum up to approximately 1000 node hours. The errors are calculated according to the mean of differences definition, c.f. equation 2.26. For this, the energy difference errors $\Delta\langle\Delta E_{i,f}\rangle$ and $\Delta\langle\Delta E_{i,s}\rangle$ were required. Their distributions were not bell-shaped, so Bayesian bootstrapping was applied. $B = 10\,000$ samples were drawn and due to the central limit theorem, the resulting distribution of mean values were normally distributed. The standard deviations of these mean distributions were used as energy difference errors.

Table 4.4: Accommodation coefficients for all surfaces. Errors in parentheses are calculated according to equation 2.26.

Surface	α_n	α_t	α_r
Baseline, Figure 4.1a	0.92(14)	0.63(6)	0.07(13)
Deposit 1, Figure 4.1b	0.87(14)	0.75(8)	-0.27(24)
Deposit 2, Figure 4.1c	0.91(19)	0.70(6)	-1.54(45)
Deposit 3, Figure 4.1d	0.86(13)	0.70(5)	0.95(10)
Deposit 4, Figure 4.1e	0.89(16)	0.69(5)	-0.70(24)
Deposit total	0.88(8)	0.71(3)	-0.24(11)

In general, the results indicate that most energy in surface normal direction is lost. Slightly more energy is retained in tangential direction. Rotational energy seems to be ambiguous with large variations between the surfaces and a slightly negative mean value. Upon comparison of the surfaces, the normal energy AC matches within the uncertainty, but is slightly lower for the deposited surfaces. This trend matches that found for the sticking probability. For the tangential energy AC, the scattering from the baseline surface was observed to retain less surface-parallel energy. It seems reasonable that scattering from a rougher surface would be more diffuse than from a flat surface. The baseline α_t value is still relatively close. This could mean that the atom-level roughness of the surface accounts for most of the dispersion of scattering angles. The rotational AC varies strongly between surfaces. Overall, it seems to be close to zero for the baseline surface and typically negative for deposited surfaces. A possible interpretation is that a rougher surface offers more impact sites where the projectile is hit off-center, a process that transfers impact energy into rotational energy.
In comparison to the estimations from temperature fits (c.f. Table 4.3), the ACs are very close. This temperature estimation method was found to be well suited to estimate ACs.

It would be suited in the situation where individual projectile information is not available but only temperatures in individual degrees of freedom. The ACs derived here may be most closely compared to data by Brann et al (c.f. Table 1.1). They did not report AC values, but they could approximately be derived from their $E_i - E_f$ plots (Figure 6 there). They found a combined translational AC of 0.98 and $\alpha_r = -0.04$. The rotational AC matches results here quite well with their model being flat and therefore closest to $\alpha_r^{\text{baseline}} = 0.07$. The combined translational ACs in this study are 0.73 for the flat and 0.75 for the rough surface. The translational AC not matching may in part be caused by their single impact angle, as α_n matches their result better than α_t.
To gain further insights into the value distributions and uncertainty, the ACs were also calculated individually for each trajectory. The resulting distributions are shown in Figure 4.3. Using them, several methods of obtaining the ACs and their uncertainties could be compared, summarized in Table 4.5. Large AC outliers were observed especially in the α_r distribution, but also for α_t. The causes for these outliers were the ones discussed in 2.3.1. Especially prominent are the high negative values in α_r. They are all cases of a projectile shifting energy from a different degree of freedom into rotational energy, leaving the surface with much more E_r than it initially had, while still having lost energy to the surface in total. The less extreme outliers ($\alpha > -60$) were caused by their respective factor of energy gain. In some cases, $E_i > E_s$ by a very small amount, causing $\Delta E_{i,s}$ to approach zero and leading to the very high negative AC values ($\alpha < 100$). High positive ACs were caused by sampled initial (mainly rotational) energies that were below E_s, causing a negative denominator in the AC, combined with gaining rotational energy (negative numerator). The closer the sampled energy is to the surface energy, the higher the AC. AC values just slightly > 1 were also observed, which were caused by cases of $E_f < E_s$. This observation showed all outliers, despite their cause, signal energy gain, although their sign and magnitude may be skewed by some value being close to E_s. It is possible that such extreme outliers rarely were encountered or reported in previous work due to the surface temperature here being so close, but not equal to zero. Yamamoto et al.[17] reported individual ACs, mentioning large outliers around a specific initial velocity value. They discarded them as numerical error.
The α_r values found in this study indicate strong coupling between translational and rotational modes. Additionally, energy was transferred into tangential translational motion, which can be as simple as a projectile entering with a near-normal angle and scattering more towards the surface-parallel direction. Both are entirely sensible scattering characteristics and the high AC values can be seen as artifacts of breaking down individual modes. Outliers for ACs of indiviual modes may reach arbitrarily high values when certain energy values coincidentally align. For such cases, the median could be a better suited method for determining the averaged AC of several trajectories. When comparing the central $5 - 95\%$ confidence intervals of the distributions with outliers (c.f. Figure 4.3) to the reported ACs, the median values match the bulk of the distribution better.
In light of the broad AC distributions, the errors calculated via the m.o.diff. approach seem to underestimate the uncertainty if many outliers are present. For α_n and α_t, it approximately covers the differences between ACs calculated via equation 2.1, the mean of the AC distribution and its median, but not for α_r. However, the bootstrap uncertainties for α_t and especially α_r are very large and rather represent the broadness of the distribution, but not the uncertainty of their mean. The SEM (c.f. 2.6.2) may be

used alternatively because it is not expected to overestimate as harshly. It is also given in Table 4.5. The SEM uncertainties are up to an order of magnitude lower than the error propagation method if no outliers are present. Going forward, uncertainties may be best reported according to the SEM if many outliers are present and with error propagation if not. Bootstrapped errors instead might be best used to quantify the extent of outliers or broadness of the distribution in lieu of histograms like in Figure 4.3.
For comparison, the errors according to the differences of means approach (c.f. equation 2.25) were calculated. As energy errors $\Delta\langle E_i\rangle$ and $\Delta\langle E_f\rangle$, the standard deviation of $B = 10^4$ Bayesian bootstrap samples of the mean were used. Additionally, it was also calculated using the SEM of the respective energy distributions. For the error of the surface energy ΔE_s, for all trajectories, the surface temperatures during the randomized pre-run were used. The standard deviation was used to approximate the extent of energy fluctuations of the thermostat which came out as approx. $\Delta T_s = 0.1\,\mathrm{K}$. Expressed as an energy, $\Delta E_s = \Delta T_s k_\mathrm{B}$. The diff.o.m errors were very high because they took into account the total broadness of the energy distributions. The respective SEM errors were the lowest overall.

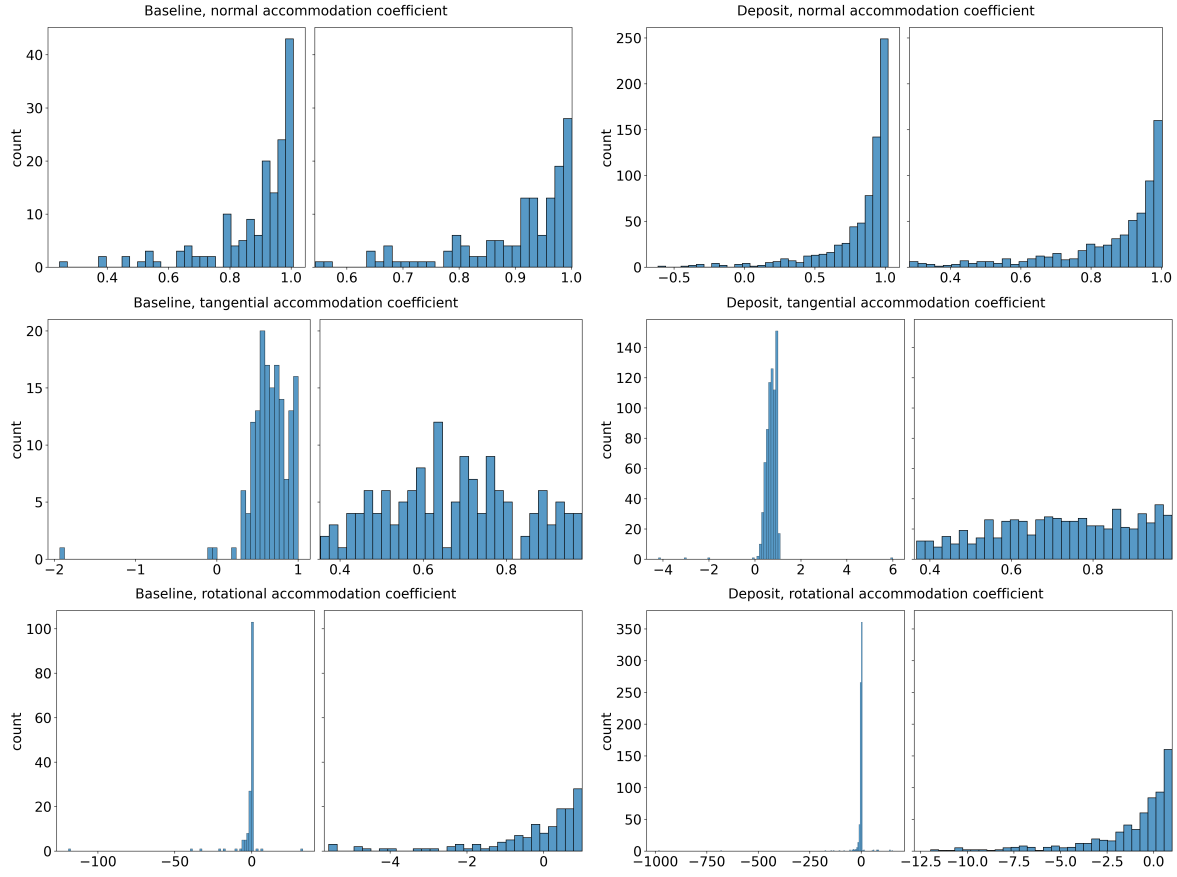

Figure 4.3: The distributions of individual ACs in the baseline model. Left column: baseline surface, right column: deposited surfaces. From top to bottom: normal, tangential, rotational energy AC. For each, the full histrogram (left) and the subset within the 5%-95% quantiles (right) are shown.

Table 4.5: Different methods to calculate ACs and their errors. To allow comparison of differences, values are given with additional significance

	Baseline			Deposit		
Parameter	α_n	α_t	α_r	α_n	α_t	α_r
Equation 2.1	0.922	0.632	0.070	0.880	0.714	-0.235
Mean of individual ACs	0.884	0.652	-1.555	0.823	0.708	-3.906
Median of individual ACs	0.935	0.678	0.219	0.927	0.734	0.214
Error propagation, m.o.diff.	0.137	0.061	0.132	0.077	0.032	0.111
Error propagation, m.o.diff., SEM	0.097	0.044	0.094	0.055	0.023	0.080
Error propagation, diff.o.m.	0.424	0.358	6.470	0.651	0.265	9.774
Error propagation, diff.o.m., SEM	0.010	0.037	0.145	0.010	0.013	0.148
Bootstrap of individual ACs	0.145	0.288	11.060	0.256	0.373	47.148
SEM of individual ACs	0.011	0.023	0.870	0.010	0.014	1.776

4.5 Energy component sampling

The practice of depositing and scattering particles by sampling random angles and velocities to estimate an ensemble with a defined temperature is common practice in the literature (c.f. Table 1.1). The clear advantage is the ease of implementation in common MD codes like LAMMPS. It was questioned how well this approximation represents a rocket motor plume ensemble. Parallel and orthogonal to the direction of propagation, it would be expected that energy components were MB-distributed. This distribution would be modified by the angle between plume propagation direction and surface normal. In this work, this angle is averaged and its distribution should not greatly modify the energy component distribution shape. The sampled initial energy in the normal and tangential modes for the 40000 trajectories in the deposit simulations are shown in Figure 4.4. The

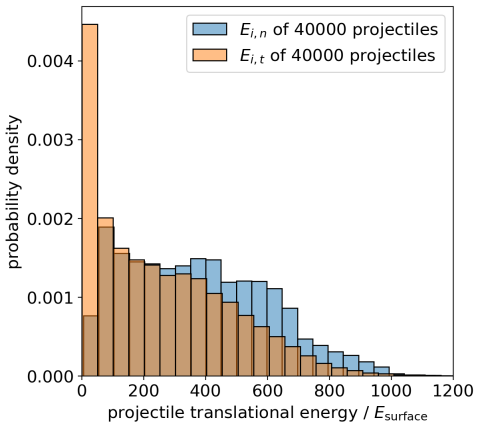

Figure 4.4: Sampled initial translational energies regardless of trajectory result

distribution is not MB-distributed. As a consequence, the definition of initial projectile

temperatures is technically incorrect. Presumably, this is caused by the sampling method of impact angles. Representing a plume ensemble correctly could be an involved problem. The aforementioned angle between plume and surface would need to be considered. However, it is not trivially known. Each simulation box features its own distribution of angles between the plume source and all walls. Whether such treatment is necessary remains to be determined for every new use case. In this study, the approximation of averaging over all impact angles equally is assumed to be sufficient.

4.6 Scattering angles

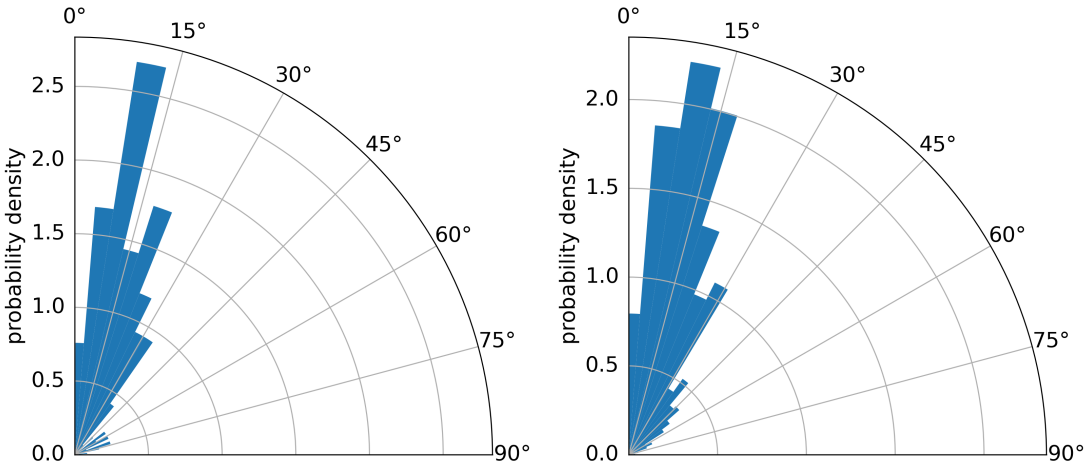

Figure 4.5: Histogram of scattering angles of the baseline model (left) and the deposited model (right).

The scattering angles of all scattered projectiles were recorded. Their distribution for both models are shown in Figure 4.5. Within statistical noise, no difference between the distributions could be discerned. This finding agrees with the similar tangential ACs found for both models. Since for the flat model α_t was slightly lower, for very large amounts of data it could be expected that the scattering distribution for the baseline would favor higher angles.

4.7 System size choice

For any scattering simulation, a choice must be made for the size of the considered section of the wall. If the wall section were too small, artifacts like artificial heating and wrapping of the shock around the periodic boundary could influence the scattering. On the other hand, an unnecessarily large wall section increases computational effort. The influence of the system size on impact dynamics was studied as described in 3.5. A broad range of sizes from $6 \times 6 \times 4$ to $18 \times 18 \times 10$ unit cells ($n_x \times n_y \times n_z$) was considered initially. The average kinetic energy at the outer box borders was monitored after the impact. A peak was visible for all sizes with a smaller amplitude the larger the size. The subset of sizes around which the peak amplitude started to plateau was selected for more detailed analysis. Combinations of z heights from 6 to 10 unit cells and xy grid sizes from 8 to 12 unit cells were considered. Simulations with a projectile velocity of $3000\,\mathrm{m\,s^{-1}}$ and

normal incidence angle ($\alpha = 0$) were performed. These parameters were chosen so that no scattering would occur. The simulations thus served as an upper bound for the impact energy that could be transferred to the surface by one projectile. All properties discussed in the following were averaged over 80 simulations that differed in the seed used for the Langevin NVT thermostat for minimization, in order to randomize the surface state.
Regarding the temperature increase, all sizes of approximately 2000 molecules or more were in the order of magnitude of $\Delta T = 1\,\mathrm{K}$. The smallest size that completely fulfilled the condition was $10 \times 10 \times 8$ with 3200 atoms and $\Delta T = 0.99\,\mathrm{K}$.
The slab was divided into a xy grid following the unit cells. The mean kinetic energy per atom in every unit cell was evaluated on this grid for the top and bottom unit cells. This grid could be visualized as an animation of the impact, with a colormap representing the average kinetic energy in a cell. The xy grid size was chosen so that in such a movie, with logarithmic scaling, the visible shock barely extended up to the boundary. This condition was reached with 10×10 unit cells.
To estimate the amount of impact energy reaching the bottom layer, the mean kinetic energy at the outermost cells from the top and bottom were compared. The z size was chosen so that this difference between the layers did not qualitatively change with increasing thickness anymore, which was the case for $n_z = 8$. All simulations from this point on were thus performed with a size of $10 \times 10 \times 8$ unit cells.

4.8 Rotational energy influence

Simulation were carried out as described in 3.6. The resulting sticking probabilities are shown in Figure 4.6. The uncertainty of sticking probabilities was estimated via Bayesian bootstrapping with $N_{\mathrm{samples}} = 400$, $B = 1000$ (c.f. 2.6.1).
It was found that the difference in sticking probability is substantial. Consequently, how the fraction of rotational energy would be sampled in the following steps was important for determining s. This result was used to inform the decision taken in 3.2. One peak at 30° where the two lines show an inversion could not be explained. Statistical noise could not be ruled out, since both points roughly lie within their respective uncertainty bands.

4.9 Error discussion

The harshest approximation in this work is arguably neglecting all species except nitrogen. Hydrogen and ammonia are expected to have a large influence on the ice structure. Additionally, the sticking probabilities and ACs for those molecules are of interest as well. Due to the scope of this master thesis, the harsh approximation was needed to develop the method and workflow, but extension to more realistic problems is needed.
There are downsides to the rigid rotor approximation used here. It is implicitly assumed that vibrational excitation does not notably change the collision process and its outcome. In further studies, a force field which allows for vibrations should be considered to confirm or deny this assumption.
There is no guarantee that the force field used here captures the scattering physics correctly, as it was not designed specifically for this purpose. To confirm, *ab initio* MD could be run with a representative test case to see whether they qualitatively or quantitatively differ. Such a test case could be done with a smaller simulation box for performance

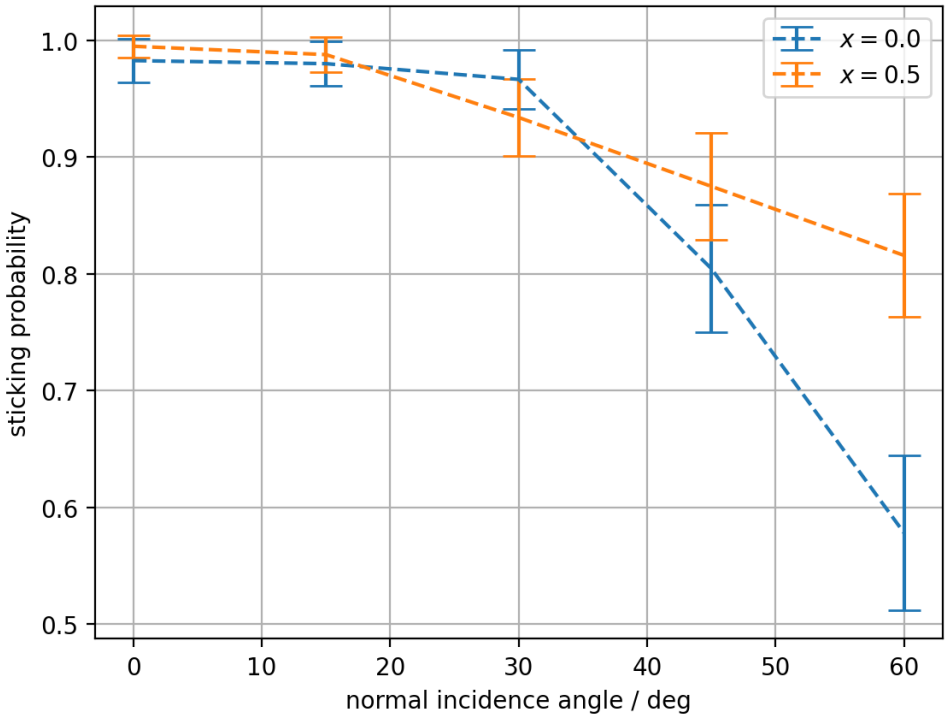

Figure 4.6: Sticking probability of selected impact angles. The total impact energy is fixed at 0.581 eV. The two lines represent simulations with all energy in translation ($x = 0$) and half of that energy in rotation ($x = 0.5$). Each data point is the average of 400 individual simulations. Error bars are estimated uncertainties from 1000 Bayesian bootstrap samples of the simulations.

reasons. This test could have two steps:

1. Minimization: whether minimization from similar starting structure would lead to the similar ice structure and lattice parameters.

2. Scattering: Using the exact same projectile properties between QM and PHAST, for a few trajectories, how much will the outcome differ?

Since the initial axis of rotation is locked to be perpendicular to the molecular bond, not all possible rotational states are covered by this method. In future work, it could be attempted to additionally sample rotational states with a lower moment of inertia.

5 Conclusions

The system of hot nitrogen gas scattering from cryogenic nitrogen ice was investigated for two models, a flat crystal and a rough deposited surface. Sticking probabilities and accommodation coefficients were determined for both models, they are summarized in Table 5.1. Using deposition to incrementally build a rough surface was extended to a polyatomic molecular ice. No prior work of MD simulations of the scattering of hot nitrogen on nitrogen was found, nor similar systems in the context of hydrazine rocket motor decomposition products on cryopump surfaces. The workflow presented here has

given special focus to determining that the system size is large enough. As a result, it was chosen much larger than what is typical in the literature.[10,13,18,26,28,29,32] Previous studies typically used simple LJ potentials. This work introduced the more sophisticated PHAST-N_2 force field with ghost sites and charge treatment to the problem.

Table 5.1: Summary of the sticking probabilities and accommodation coefficients determined in this work. Results from literature are compared. The most applicable system or condition was chosen for comparison when several were included in the studies.

Model	T_s / K	s	α_n	α_t	α_r
Baseline	4.3	0.984(3)	0.92(14)	0.63(6)	0.07(13)
Deposited	4.3	0.982(2)	0.88(8)	0.71(3)	-0.24(11)
Bisschop et al.[78]	14	≥ 0.85	–	–	–
Thompson et al.[79]	33.5	0.90	–	–	–
Brann et al.[36] experiment	20	0.97	–	–	–
Brann et al.[36] MD[a]	20	0.91	0.89[b]		11
Mehta et al.[10][c]	300	0.3	1.06	0.87	–

[a] Inferred from their reported E_i and E_f.
[b] They only report a combined translational AC.
[c] They report the values for different impact angles, the mean is given here. The sticking probability was reported for their 1100 m s^{-1} data set and the ACs for their 750 m s^{-1} data set.

The determined sticking probabilities generally match literature values for cold surfaces. They may be interpreted as an upper boundary due to the approximations taken. Scattering was shown to be possible and the assumption of the whole plume freezing out to be inexact. In comparison to a study concerning a 300 K surface (Mehta et al.[10]), the sticking probability differs significantly. This highlights the importance of similar surface temperature for meaningful comparison of these parameters.
Not many ACs were reported in literature that represent similar physical systems. In the one that does (Brann et al.[36]), the rotational AC matches in the sense that it suggests energy is transferred from translational to rotational modes. The high value is a consequence of them setting the initial rotational energy to zero and the very low surface temperature. While they only report a combined translational AC, it qualitatively fits this study's results. The trend of a higher normal than tangential AC matches the results from Mehta et al..[10] They indicate that especially tangential momentum is partially conserved upon scattering. It shows that the often taken approximation of fully diffuse scattering may be inappropriate for the system of the STG-CT. In general, the obtained parameters are expected to be an improvement over the previous assumption in DSMC simulations of the STG-CT with $s = 1$ and therefore no scattering kernel.[80]
In future work, the workflow should be extended to consider more species. Mixed nitrogen/hydrogen could be formed using the deposition method. First results have shown that challenges arise with high hydrogen concentrations. The resulting ices were less crystalline and showed severely lowered thermal conductivity, limiting cooling efficiency of the thermal layers. For deposition of such surfaces, the cooling scheme between impacts would need to be extended. Such extensions could involve applying the thermostat to portions

of the aggregate between impacts. Furthermore, the definition of the hydrogen concentration becomes slightly ambiguous. One fraction is defined for the sampling of projectiles, but the concentration in the surface is affected by both the differing sticking probabilities and sputtering yields between N_2 and H_2. The scattering simulations could be performed using hydrogen as projectile to obtain the same parameters for this species as well. In preliminary results, the sticking probability for hydrogen on N_2 and mixed ices was found to be still high. Similarly, ammonia could be incorporated into plume and ice. Extending the work to bipropellant rocket motors should be possible by using higher velocities and energies and exchanging the respective main combustion products.
The CLL kernel parametrized here or other methods that can utilize the MD data could be used to simulate the STG-CT with DSMC. A comparison of the results compared to previous work[80] could show whether the *ab initio* determined sticking probability and ACs are advantageous. Future work could also focus on improving the technique of sampling velocity vectors from a plume ensemble.

References

[1] R. E. Alt, "Bipropellant Engine Plume Contamination Program Volume I Chamber Measurements - Phase I", *AEDC US Air Force* **1979**.

[2] C. E. Soares, W. A. Hoey, A. T. Wong, M. Grabe in 51st Annual Lunar and Planetary Science Conference, **2020**, p. 3066.

[3] In Proceedings of International Symposium on"SM/MPAC\&SEED Experiment, in collab. with N. Baba, Y. Kimoto, **2008**.

[4] F. G. ETHERIDGE, R. A. BOUDREAUX, "Attitude-Control Rocket Exhaust Plume Effects on Spacecraft Functional Surfaces", *Journal of Spacecraft and Rockets* **2012**, DOI 10.2514/3.29861.

[5] M. Grabe, "STG-CT: High-vacuum Plume Test Facility for Chemical Thrusters", *Journal of large-scale research facilities JLSRF* **2016**, *2*, A86–A86.

[6] T. W. Price, D. D. Evans, The Status of Monopropellant Hydrazine Technology, Contractor Report JPL-TR-32-1227, NASA, Jet Propulsion Lab, **1968**.

[7] G. A. Bird, "Approach to Translational Equilibrium in a Rigid Sphere Gas", *The Physics of Fluids* **1963**, *6*, 1518–1519.

[8] G. A. Bird, "Molecular Gas Dynamics", *NASA STI/Recon Technical Report A* **1976**, *76*, 40225.

[9] G. A. Bird, *Molecular Gas Dynamics And The Direct Simulation Of Gas Flows*, Oxford University Press, **1994**.

[10] N. A. Mehta, D. A. Levin, "Molecular-Dynamics-Derived Gas–Surface Models for Use in Direct-Simulation Monte Carlo", *Journal of Thermophysics and Heat Transfer* **2017**, *31*, 757–771.

[11] C. Cercignani, M. Lampis, "Kinetic Models for Gas-Surface Interactions", *Transport Theory and Statistical Physics* **1971**, *1*, 101–114.

[12] R. G. Lord, "Some Extensions to the Cercignani–Lampis Gas–Surface Scattering Kernel", *Physics of Fluids A: Fluid Dynamics* **1991**, *3*, 706–710.

[13] J. Blömer, A. E. Beylich, "Molecular Dynamics Simulation of Energy Accommodation of Internal and Translational Degrees of Freedom at Gas–Surface Interfaces", *Surface Science* **1999**, *423*, 127–133.

[14] K. Bolton, M. Svanberg, J. B. C. Pettersson, "Classical Trajectory Study of Argon–Ice Collision Dynamics", *The Journal of Chemical Physics* **1999**, *110*, 5380–5391.

[15] N. Yamanishi, Y. Matsumoto, K. Shobatake, "Multistage Gas–Surface Interaction Model for the Direct Simulation Monte Carlo Method", *Physics of Fluids* **1999**, *11*, 3540–3552.

[16] D. Bruno, M. Cacciatore, S. Longo, M. Rutigliano, "Gas-Surface Scattering Models for Particle Fluid Dynamics: A Comparison between Analytical Approximate Models and Molecular Dynamics Calculations", *Chemical Physics Letters* **2000**, *320*, 245–254.

[17] K. Yamamoto, H. Takeuchi, T. Hyakutake, "Scattering Properties and Scattering Kernel Based on the Molecular Dynamics Analysis of Gas-Wall Interaction", *Physics of Fluids* **2007**, *19*, 087102.

[18] K. Yamamoto, H. Takeuchi, T. Hyakutake, "Characteristics of Reflected Gas Molecules at a Solid Surface", *Physics of Fluids* **2006**, *18*, 046103.

[19] K. J. Daun, "Thermal Accommodation Coefficients between Polyatomic Gas Molecules and Soot in Laser-Induced Incandescence Experiments", *International Journal of Heat and Mass Transfer* **2009**, *52*, 5081–5089.

[20] P. Spijker, A. J. Markvoort, S. V. Nedea, P. A. J. Hilbers, "Computation of Accommodation Coefficients and the Use of Velocity Correlation Profiles in Molecular Dynamics Simulations", *Physical Review E* **2010**, *81*, 011203.

[21] T. T. Pham, Q. D. To, G. Lauriat, C. Léonard, V. V. Hoang, "Effects of Surface Morphology and Anisotropy on the Tangential-Momentum Accommodation Coefficient between Pt(100) and Ar", *Physical Review E* **2012**, *86*, 051201.

[22] T. Liang, Q. Li, W. Ye, "Performance Evaluation of Maxwell and Cercignani-Lampis Gas-Wall Interaction Models in the Modeling of Thermally Driven Rarefied Gas Transport", *Physical Review E* **2013**, *88*, 013009.

[23] M. Hossein Gorji, P. Jenny, "A Gas-Surface Interaction Kernel for Diatomic Rarefied Gas Flows Based on the Cercignani-Lampis-Lord Model", *Physics of Fluids* **2014**, *26*, 122004.

[24] J. Reinhold, T. Veltzke, B. Wells, J. Schneider, F. Meierhofer, L. Colombi Ciacchi, A. Chaffee, J. Thöming, "Molecular Dynamics Simulations on Scattering of Single Ar, N2, and CO2 Molecules on Realistic Surfaces", *Computers & Fluids* **2014**, *97*, 31–39.

[25] N. A. Mehta, D. A. Levin, V. J. Murray, T. K. Minton, "Study of Non-Reactive Scattering from Graphene Using Molecular Beam Experiments and Molecular Dynamics", *AIP Conference Proceedings* **2016**, *1786*, 100003.

[26] N. Andric, P. Jenny, "Molecular Dynamics Investigation of Energy Transfer during Gas-Surface Collisions", *Physics of Fluids* **2018**, *30*, 077104.

[27] T. Liang, Q. Li, W. Ye, "A Physical-Based Gas–Surface Interaction Model for Rarefied Gas Flow Simulation", *Journal of Computational Physics* **2018**, *352*, 105–122.

[28] M. Liao, Q.-D. To, C. Léonard, V. Monchiet, "Non-Parametric Wall Model and Methods of Identifying Boundary Conditions for Moments in Gas Flow Equations", *Physics of Fluids* **2018**, *30*, 032008.

[29] N. Andric, D. W. Meyer, P. Jenny, "Data-Based Modeling of Gas-Surface Interaction in Rarefied Gas Flow Simulations", *Physics of Fluids* **2019**, *31*, 067109.

[30] S. Yousefi-Nasab, J. Safdari, J. Karimi-Sabet, A. Norouzi, E. Amini, "Determination of Momentum Accommodation Coefficients and Velocity Distribution Function for Noble Gas-Polymeric Surface Interactions Using Molecular Dynamics Simulation", *Applied Surface Science* **2019**, *493*, 766–778.

[31] T. Liang, J. Zhang, Q. Li, "A Parameter-Free Physical Model for Gas–Surface Interaction", *Physics of Fluids* **2021**, *33*, 082005.

[32] W. Liu, J. Zhang, Y. Jiang, L. Chen, C.-H. Lee, "DSMC Study of Hypersonic Rarefied Flow Using the Cercignani–Lampis–Lord Model and a Molecular-Dynamics-Based Scattering Database", *Physics of Fluids* **2021**, *33*, 072003.

[33] S. M. Nejad, E. Iype, A. Frijns, D. Smeulders, "Modeling Rarefied Gas-Solid Surface Interactions for Couette Flow with Different Wall Temperatures Using an Unsupervised Machine Learning Technique", *Physical Review E* **2021**, *104*, 015309.

[34] S. M. Nejad, S. Nedea, A. Frijns, D. Smeulders, "Development of a Scattering Model for Diatomic Gas–Solid Surface Interactions by an Unsupervised Machine Learning Approach", *Physics of Fluids* **2022**, *34*, 117122.

[35] H. (Wu, W. (Chen, Z. (Jiang, "Gaussian Mixture Models for Diatomic Gas−surface Interactions under Thermal Non-Equilibrium Conditions", *Physics of Fluids* **2022**, *34*, 082007.

[36] M. R. Brann, X. Ma, S. J. Sibener, "Isotopic Enrichment Resulting from Differential Condensation of Methane Isotopologues Involving Non-equilibrium Gas–Surface Collisions Modeled with Molecular Dynamics Simulations", *The Journal of Physical Chemistry C* **2023**, *127*, 13286–13294.

[37] Z. Wang, C. Song, F. Qin, X. Luo, "Establishing a Data-Based Scattering Kernel Model for Gas–Solid Interaction by Molecular Dynamics Simulation", *Journal of Fluid Mechanics* **2021**, *928*, A34.

[38] Y. Yamashita, M. Kato, M. Arakawa, "Experimental Study on the Rheological Properties of Polycrystalline Solid Nitrogen and Methane: Implications for Tectonic Processes on Triton", *Icarus* **2010**, *207*, 972–977.

[39] S. Brunauer, L. S. Deming, W. E. Deming, E. Teller, "On a Theory of the van Der Waals Adsorption of Gases", *Journal of the American Chemical Society* **1940**, *62*, 1723–1732.

[40] S. J. Plimpton, S. G. Moore, A. Borner, A. K. Stagg, T. P. Koehler, J. R. Torczynski, M. A. Gallis, "Direct Simulation Monte Carlo on Petaflop Supercomputers and Beyond", *Physics of Fluids* **2019**, *31*, 086101.

[41] G. Govindaraj, M. Ganesan, "The Chemically Reacting Hypersonic Flow over a Reentry Capsule with Hybrid Chemical Reaction Models", *AIP Conference Proceedings* **2024**, *2996*, 150004.

[42] J. F. Padilla, I. D. Boyd, "Assessment of Gas-Surface Interaction Models for Computation of Rarefied Hypersonic Flow", *Journal of Thermophysics and Heat Transfer* **2009**, *23*, 96–105.

[43] Q.-D. To, V.-H. Vu, G. Lauriat, C. Léonard, "Boundary Conditions for Gas Flow Problems from Anisotropic Scattering Kernels", *Journal of Mathematical Physics* **2015**, *56*, 103101.

[44] D. A. King, M. G. Wells, "Molecular Beam Investigation of Adsorption Kinetics on Bulk Metal Targets: Nitrogen on Tungsten", *Surface Science* **1972**, *29*, 454–482.

[45] E. Matar, H. Bergeron, F. Dulieu, H. Chaabouni, M. Accolla, J. L. Lemaire, "Gas Temperature Dependent Sticking of Hydrogen on Cold Amorphous Water Ice Surfaces of Interstellar Interest", *The Journal of Chemical Physics* **2010**, *133*, 104507.

[46] M. E. Tuckerman, *Statistical Mechanics: Theory and Molecular Simulation*, Oxford University Press, **2023**, 881 pp.

[47] D. Frenkel, B. Smit, *Understanding Molecular Simulation: From Algorithms to Applications*, Elsevier, **2023**, 868 pp.

[48] T. Darden, D. York, L. Pedersen, "Particle Mesh Ewald: An N log(N) Method for Ewald Sums in Large Systems", *The Journal of Chemical Physics* **1993**, *98*, 10089–10092.

[49] C. R. Cioce, K. McLaughlin, J. L. Belof, B. Space, "A Polarizable and Transferable PHAST N2 Potential for Use in Materials Simulation", *Journal of Chemical Theory and Computation* **2013**, *9*, 5550–5557.

[50] M. Waldman, A. Hagler, "New Combining Rules for Rare Gas van Der Waals Parameters", *Journal of Computational Chemistry* **1993**, *14*, 1077–1084.

[51] L. Verlet, "Computer "Experiments" on Classical Fluids. I. Thermodynamical Properties of Lennard-Jones Molecules", *Physical Review* **1967**, *159*, 98–103.

[52] W. C. Swope, H. C. Andersen, P. H. Berens, K. R. Wilson, "A Computer Simulation Method for the Calculation of Equilibrium Constants for the Formation of Physical Clusters of Molecules: Application to Small Water Clusters", *The Journal of Chemical Physics* **1982**, *76*, 637–649.

[53] H. J. C. Berendsen, J. P. M. Postma, W. F. van Gunsteren, A. DiNola, J. R. Haak, "Molecular Dynamics with Coupling to an External Bath", *The Journal of Chemical Physics* **1984**, *81*, 3684–3690.

[54] S. C. Harvey, R. K.-Z. Tan, T. E. Cheatham III, "The Flying Ice Cube: Velocity Rescaling in Molecular Dynamics Leads to Violation of Energy Equipartition", *Journal of Computational Chemistry* **1998**, *19*, 726–740.

[55] R. W. Pastor in *The Molecular Dynamics of Liquid Crystals*, (Eds.: G. R. Luckhurst, C. A. Veracini), Springer Netherlands, Dordrecht, **1994**, pp. 85–138.

[56] G. J. Martyna, M. L. Klein, M. Tuckerman, "Nosé–Hoover Chains: The Canonical Ensemble via Continuous Dynamics", *The Journal of Chemical Physics* **1992**, *97*, 2635–2643.

[57] B. J. Leimkuhler, C. R. Sweet, "The Canonical Ensemble via Symplectic Integrators Using Nosé and Nosé–Poincaré Chains", *The Journal of Chemical Physics* **2004**, *121*, 108–116.

[58] H. Kamberaj, R. J. Low, M. P. Neal, "Time Reversible and Symplectic Integrators for Molecular Dynamics Simulations of Rigid Molecules", *The Journal of Chemical Physics* **2005**, *122*, 224114.

[59] G. J. Martyna, D. J. Tobias, M. L. Klein, "Constant Pressure Molecular Dynamics Algorithms", *The Journal of Chemical Physics* **1994**, *101*, 4177–4189.

[60] B. Efron, "Bootstrap Methods: Another Look at the Jackknife", *The Annals of Statistics* **1979**, *7*, 1–26.

[61] K. Kelley, "The Effects of Nonnormal Distributions on Confidence Intervals Around the Standardized Mean Difference: Bootstrap and Parametric Confidence Intervals", *Educational and Psychological Measurement* **2005**, *65*, 51–69.

[62] D. B. Rubin, "The Bayesian Bootstrap", *The Annals of Statistics* **1981**, *9*, 130–134.

[63] A. P. Thompson, H. M. Aktulga, R. Berger, D. S. Bolintineanu, W. M. Brown, P. S. Crozier, P. J. in 't Veld, A. Kohlmeyer, S. G. Moore, T. D. Nguyen, et al., "LAMMPS - a Flexible Simulation Tool for Particle-Based Materials Modeling at the Atomic, Meso, and Continuum Scales", *Computer Physics Communications* **2022**, *271*, 108171.

[64] T. F. Miller, III, M. Eleftheriou, P. Pattnaik, A. Ndirango, D. Newns, G. J. Martyna, "Symplectic Quaternion Scheme for Biophysical Molecular Dynamics", *The Journal of Chemical Physics* **2002**, *116*, 8649–8659.

[65] D. S. Cerutti, R. E. Duke, T. A. Darden, T. P. Lybrand, "Staggered Mesh Ewald: An Extension of the Smooth Particle-Mesh Ewald Method Adding Great Versatility", *Journal of Chemical Theory and Computation* **2009**, *5*, 2322–2338.

[66] A. Neelov, C. Holm, "Interlaced P3M Algorithm with Analytical and Ik-Differentiation", *The Journal of Chemical Physics* **2010**, *132*, 234103.

[67] R. W. Hockney, J. W. Eastwood, *Computer Simulation Using Particles*, CRC Press, **2021**.

[68] C. R. Harris, K. J. Millman, S. J. van der Walt, R. Gommers, P. Virtanen, D. Cournapeau, E. Wieser, J. Taylor, S. Berg, N. J. Smith, et al., "Array Programming with NumPy", *Nature* **2020**, *585*, 357–362.

[69] P. Virtanen, R. Gommers, T. E. Oliphant, M. Haberland, T. Reddy, D. Cournapeau, E. Burovski, P. Peterson, W. Weckesser, J. Bright, et al., "SciPy 1.0: Fundamental Algorithms for Scientific Computing in Python", *Nature Methods* **2020**, *17*, 261–272.

[70] N. Michaud-Agrawal, E. J. Denning, T. B. Woolf, O. Beckstein, "MDAnalysis: A Toolkit for the Analysis of Molecular Dynamics Simulations", *Journal of Computational Chemistry* **2011**, *32*, 2319–2327.

[71] R. J. Gowers, M. Linke, J. Barnoud, T. J. E. Reddy, M. N. Melo, S. L. Seyler, J. Domański, D. L. Dotson, S. Buchoux, I. M. Kenney, et al., "MDAnalysis: A Python Package for the Rapid Analysis of Molecular Dynamics Simulations", *Proceedings of the 15th Python in Science Conference* **2016**, 98–105.

[72] J. D. Hunter, "Matplotlib: A 2D Graphics Environment", *Computing in Science & Engineering* **2007**, *9*, 90–95.

[73] U. Ganzer, *Gasdynamik*, Springer-Verlag, **2013**, 346 pp.

[74] S. Yamazaki, M. Taki, Y. Fujitani, "Rotational Relaxation in Free Jet Expansion for N2 from 300 to 1000 K", *The Journal of Chemical Physics* **1981**, *74*, 4476–4479.

[75] G. A. Bird, "Breakdown of Translational and Rotational Equilibrium in Gaseous Expansions", *AIAA Journal* **1970**, *8*, 1998–2003.

[76] R. W. G. Wyckoff, "Nitrogen, Sample at T = 4.2 K", *Crystal Structures* **1963**, *1*, 7–83.

[77] A. I. Jewett, D. Stelter, J. Lambert, S. M. Saladi, O. M. Roscioni, M. Ricci, L. Autin, M. Maritan, S. M. Bashusqeh, T. Keyes, et al., "Moltemplate: A Tool for Coarse-Grained Modeling of Complex Biological Matter and Soft Condensed Matter Physics", *Journal of Molecular Biology*, Computation Resources for Molecular Biology **2021**, *433*, 166841.

[78] S. E. Bisschop, H. J. Fraser, K. I. Öberg, E. F. van Dishoeck, S. Schlemmer, "Desorption Rates and Sticking Coefficients for CO and N2 Interstellar Ices", *Astronomy & Astrophysics* **2006**, *449*, 1297–1309.

[79] R. S. Thompson, M. R. Brann, S. J. Sibener, "Sticking Probability of High-Energy Methane on Crystalline, Amorphous, and Porous Amorphous Ice Films", *The Journal of Physical Chemistry C* **2019**, *123*, 17855–17863.

[80] M. Grabe, A. Holz, S. Ziegenhagen, K. Hannemann, "Numerical Investigation of Two Interacting Parallel Thruster-Plumes and Comparison to Experiment", *AIP Conference Proceedings* **2014**, *1628*, 581–588.

[81] N. Fray, B. Schmitt, "Sublimation of Ices of Astrophysical Interest: A Bibliographic Review", *Planetary and Space Science* **2009**, *57*, 2053–2080.

6 Appendix

6.1 N_2 vapor pressure

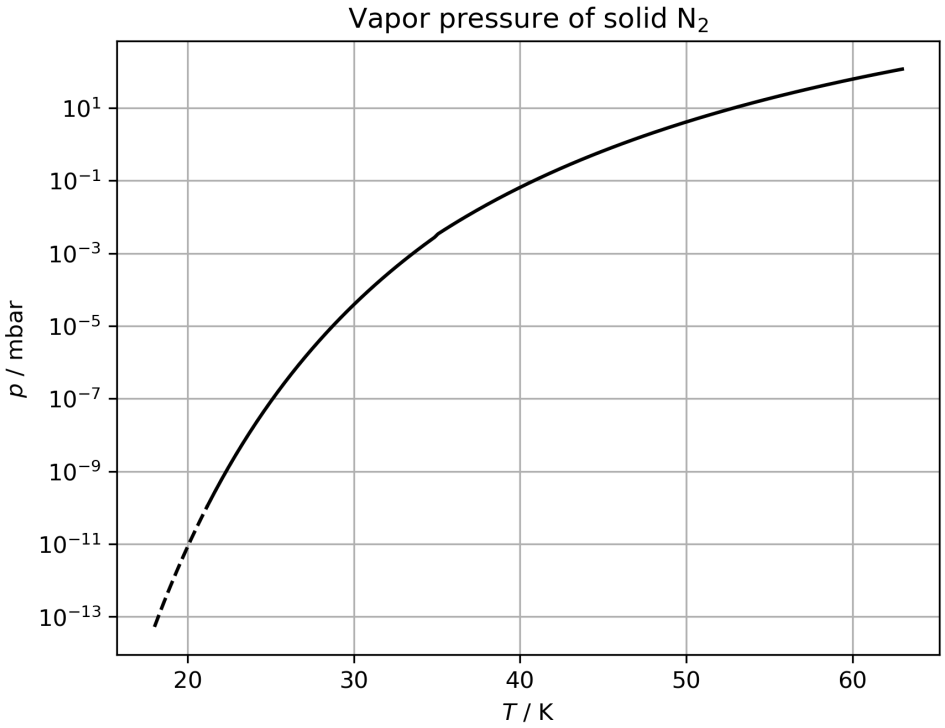

Figure 6.1: Vapor pressure of solid nitrogen as determined by Fray et al.[81] (solid line), extrapolated to the region below21.2 K to 18 K.

6.2 Accommodation coefficient codomain

Table 6.1: Some exemplary values the AC can take and their cause. Values given in arbitrary units. Comments are from the frame of reference of the projectile, not the surface.

Relation	E_i	E_f	E_s	α	comment
$E_i = E_f < E_s$	1	1	2	1	specular reflection from hotter surface
$E_i = E_f > E_s$	2	2	1	1	specular reflection from colder surface
$E_f = E_s < E_s$	1	2	2	1	diffuse reflection from hotter surface
$E_f = E_s > E_s$	2	1	1	1	diffuse reflection from colder surface
$E_i < E_f < E_s$	1	2	3	0.5	partial accommodation to hotter surface
$E_i < E_f > E_s$	1	3	2	2	energy gain beyond surface energy
$E_i < E_f > E_s$	2	3	1	-1	energy gain despite colder surface
$E_i > E_f < E_s$	2	1	3	-1	energy loss despite hotter surface
$E_i > E_f < E_s$	3	1	2	2	energy loss beyond surface energy
$E_i > E_f > E_s$	3	2	1	0.5	partial accommdoation to colder surface

6.3 Simulation details

Table 6.2: The physical and simulation settings used for the parametrization of the baseline model. All distributions given are sampled random uniform, except stated otherwise like for the temperatures. Thermostats are Nosé-Hoover if not stated otherwise.

Type	Parameter	Value
physical	Surface temperature T_s	4.3 K
	Surface structure	α-N_2 $\left(Pa\overline{3}\right)$
	Gas translation temperature T_s	122 K
	Gas rotational temperature T_s	159 K
	Plume base velocity v_stream	$1259\,\mathrm{m\,s^{-1}}$
	Incidence polar angles	0°–75°
	Incidence azimuth angles	0°–360°
	Projectile impact position	Random full surface
simulation	System size	$10 \times 10 \times 8$ unit cells
	Initial simulation box size	56 Å × 56 Å × 96.4 Å
	Relaxed box width l_x/l_y	55.261 Å
	Periodic boundary conditions	full periodicity
	Minimization scheme	5 ps Langevin NVT + 5 ps NPT
	Randomization pre-run	10 ps + 0–50 ps NVE
	Time step size Δt	1 fs
	Interaction cutoff distance	8 Å
	Long range Coulomb solver	pppm/stagger[65–67] 10^{-6}
	Sticking criterion	$\langle V_\mathrm{proj}\rangle < -0.5\,\mathrm{kcal\,mol^{-1}}$ & $\langle E_\mathrm{kin}\rangle < 0.2\,\mathrm{kcal\,mol^{-1}}$
	Number of simulations averaged	10 000
	Impact simulation length t_max	50 ps
	Trajectory files saved	no

Table 6.3: The physical and simulation settings used for the parametrization of the deposited model. All distributions given are sampled random uniform, except stated otherwise like for the temperatures. Thermostats are Nosé-Hoover if not stated otherwise.

Type	Parameter	Value
physical	Surface temperature T_s	4.3 K
	Surface structure	deposited surfaces
	Gas translation temperature T_s	122 K
	Gas rotational temperature T_s	159 K
	Plume base velocity v_stream	$1259\,\mathrm{m\,s^{-1}}$
	Incidence polar angles	0°–75°
	Incidence azimuth angles	0°–360°
	Projectile impact position	Random full surface
simulation	System size	$10 \times 10 \times 8$ unit cells
	Initial simulation box size	56 Å × 56 Å × 96.4 Å
	Relaxed box width l_x/l_y	55.63 Å, 55.63 Å, 55.63 Å, 55.5439 Å,
	Periodic boundary conditions	full periodicity
	Minimization scheme	5 ps Langevin NVT + 5 ps NPT
	Randomization pre-run	10 ps + 0–50 ps NVE
	Time step size Δt	1 fs
	Interaction cutoff distance	8 Å
	Long range Coulomb solver	pppm/stagger[65–67] 10^{-6}
	Sticking criterion	$\langle V_\mathrm{proj}\rangle < -0.5\,\mathrm{kcal\,mol^{-1}}$ & $\langle E_\mathrm{kin}\rangle < 0.2\,\mathrm{kcal\,mol^{-1}}$
	Number of simulations averaged	$4 \times 10\,000$
	Impact simulation length t_max	50 ps
	Trajectory files saved	no

Table 6.4: The physical and simulation settings used for the test of the influence of projectile rotational energy. Thermostats are Nosé-Hoover if not stated otherwise.

Type	Parameter	Value
physical	Surface temperature T_s	4.3 K
	Surface structure	α-N_2 $\left(Pa\overline{3}\right)$
	Plume base velocity v_{stream}	$2000\,m\,s^{-1}$
	Rotational energy	[0 eV, 0.29 eV]
	Incidence polar angles	[0, 15, 30, 45, 60]
	Incidence azimuth angles	0°–360°
	Projectile impact position	central $5.6 \times 5.6\,Å^2$
simulation	System size	$10 \times 10 \times 8$ unit cells
	Initial simulation box size	$56\,Å \times 56\,Å \times 62.8\,Å$
	Periodic boundary conditions	full periodicity
	Minimization scheme	5 ps Langevin NVT + 5 ps NPT + 10 ps NVE
	Randomization pre-run	none
	Time step size Δt	1 fs
	Interaction cutoff distance	8 Å
	Long range Coulomb solver	pppm/stagger[65–67] 10^{-6}
	Sticking criterion	$\langle V_{proj} \rangle + \langle E_{kin} \rangle < 1.59\,kcal\,mol^{-1}$
	Number of simulations averaged	400
	Impact simulation length t_{max}	50 ps
	Trajectory files saved	yes

Table 6.5: The physical and simulation settings used for the test of the influence of the system size. Thermostats are Nosé-Hoover if not stated otherwise.

Type	Parameter	Value
physical	Surface temperature T_s	4.3 K
	Surface structure	α-N_2 $\left(Pa\overline{3}\right)$
	Plume base velocity v_{stream}	3000 m s^{-1}
	Rotational energy	0 eV
	Incidence polar angles	0°
	Incidence azimuth angles	–
	Projectile impact position	exact xy-center
simulation	System size	Various
	Initial simulation box size	Various, 5.6 Å^3 per unit cell
	Periodic boundary conditions	full periodicity
	Minimization scheme	2 ps Langevin NVT + 18 ps NVT + 10 ps NVE
	Randomization pre-run	none
	Time step size Δt	1 fs
	Interaction cutoff distance	8 Å
	Long range Coulomb solver	pppm/stagger[65–67] 10^{-6}
	Sticking criterion	none
	Number of simulations averaged	80
	Impact simulation length t_{max}	50 ps
	Trajectory files saved	yes